Linear analysis of the
influence of neutronic-thermal-hydraulic coupling on the stability of a natural convection driven supercritical water loop

Alistair Zonneveld

TU Delft
Delft
University of
Technology

Challenge the future

Linear analysis of the influence of neutronic-thermal-hydraulic coupling on the stability of a natural convection driven supercritical water loop

by

Alistair Zonneveld

in partial fulfillment of the requirements for the degree of

Bachelor of Science
in Applied Physics

at Delft University of Technology

Supervisor: Dr. ir. M. Rohde
Thesis committee: J.J. Derksen

An electronic version of this thesis is available at http://repository.tudelft.nl/.

TUDelft Delft
University of
Technology

Nomenclature

Roman characters

A	[m^2]	Channel flow area
A_w	[m^2]	Wall cross-sectional area
C_i	[m^{-3}]	Precursor concentration
D_H	[m]	Hydraulic diameter
E_f	[J]	Energy per fission event
H	[J kg^{-1}]	Specific enthalpy
K		Pressure loss coefficient
L	[m]	Length
M	[g mol^{-1}]	Molar mass
N	[m^{-3}]	Number density
N_A	[mol^{-1}]	Avogadro constant
P_{in}	[m]	Perimeter
Q	[J s^{-1}]	Core heating power
Q_w	[J s^{-1}]	Fuel-to-wall heat flow
$\mathcal{R}$		Reactivity
T	[K]	Temperature
V	[m^3]	Volume
V_f	[m^3]	Fuel volume
W	[kg s^{-1}]	Mass flow rate
c_p	[J kg^{-1} K^{-1}]	Fluid specific heat
$c_{p,w}$	[J kg^{-1} K^{-1}]	Wall material specific heat
f		Darcy friction factor
g	[ms^{-2}]	Gravitational acceleration
h	[J kg^{-1}]	Specific enthalpy
n	[m^{-3}]	Neutron concentration
p	[N m^{-2}]	Pressure
t	[s]	Time
v_n	[ms^{-1}]	Neutron velocity

Greek characters

Λ	[s]	Mean generation time
Σ_f	[m^{-1}]	Macroscopic neutronic cross-section for thermal fission
α_r	[m^3 kg^{-1}]	Density reactivity feedback coefficient
β		Delayed neutron fraction
ε		Enrichment
θ	[K]	Temperature perturbation
λ		Eigenvalue
λ_f	[J s^{-1} m^{-1} K^{-1}]	Fluid thermal conductivity
λ_i	[s^{-1}]	Precursor decay constant
λ_w	[J s^{-1} m^{-1} K^{-1}]	Wall thermal conductivity
μ	[N s m^{-2}]	Dynamic viscosity
ρ	[kg m^{-3}]	Density
ρ_w	[kg m^{-3}]	Wall material density
σ_f	[m^{-3}]	Microscopic neutronic cross-section for thermal fission
τ	[s]	Fuel heat transfer time constant

υ	$[\text{m}^3 \text{ kg}^{-1}]$	Fluid specific volume

Dimensionless numbers

N_{Fr}		Froude number
N_{sub}		Subcooling number
$N_{\Delta h}$		Pseudo phase change number
Nu		Nusselt number

Subscripts — Value taken at:

0	Bottom core node
1	Top core node
B	Buffer vessel node
D	Downcomer node
F	Fuel node
R	Riser node
pc	Pseudo-critical point
w	Wall node (low heating model)
$w,0$	Bottom wall node (high heating model)
$w,1$	Top wall node (high heating model)

Other

$\overline{X}$		Steady state value of variable
$\underline{X}$		Dimensionless variable
$\check{x}$		Perturbation

$\widehat{Nu}$	$[\text{J}^{0.66} \text{ s}^{-0.66} \text{ m}^{-0.66} \text{ K}^{-0.66}]$	Adjusted Nusselt number

Common abbreviations

BWR	Boiling Water Reactor
GIF	Generation IV International Forum
HPLWR	High Performance Light Water Reactor
NIST	National Institute of Standards and Technology
NSB	Neutral Stability Boundary
PWR	Pressurised Water Reactor
SCWR	Supercritical Water Reactor

Abstract

The High Performance Light Water Reactor (HPLWR) is a European-designed reactor based on the Supercritical-Water-Cooled Reactor (SCWR) concept, one of the six Generation IV reactor concepts. The HPLWR is designed to be more efficient, more environmentally friendly, and more inherently safe than pre-existing reactor designs based on light water. At Delft University of Technology, a natural convection driven variant of the HPLWR is being researched. To ensure the viability of the design, stability issues must be investigated first. A computational model exists for calculating the stability of the natural circulation driven HPLWR. In this thesis, that model is extended with the inclusion of neutronic-thermal-hydraulic coupling.

In the model, the reactor is simplified to a handful of nodes. For each node, conservation balances are set up for mass, heat and momentum. The balance equations are linearised, and the system is reduced to an eigenvalue problem. Steady-state conditions of the system are found using an iterative process. The results are displayed as a map of stable and unstable regions on a nondimensional plane of operating conditions.

The implementation of neutronic-thermal-hydraulic coupling is found to have a destabilising effect. The destabilising effect diminishes for very large values of the fuel heat transfer model time constant; beyond $\tau \approx 100$ s. A new unstable region is found adjacent to a region from previous results, with similar characteristics. A parametric study is performed to investigate the influence of various design parameters.

Frequency analysis shows that an instability domain previously thought only to contain Ledinegg instabilities exhibits dynamic instabilities as well. Ledinegg instabilities are found in the same regions as in previous investigations, but not in the newly found unstable area.

This thesis is a continuation of work by Krijger [1] and Lippens [2], who did previous work on the computational model used.

Contents

1

Introduction

1.1. Background

As the world's wealth, population, and technological prowess have increased, so has the demand for the power to sustain these trends. Accomodating this need is one of mankind's biggest challenges of today. Much of the world's power, be it for heating, traffic, or industrial use, is produced by the combustion of fossil fuels, which produces carbon dioxide (CO_2). As CO_2 is one of the leading causes of global warming, methods of generating power without emitting it are increasingly becoming a necessity.

In 2009, over 400 nuclear power reactors, mostly Boiling Water Reactors (BWR) and Pressurised Water Reactors (PWR) were in operation, producing electrical power for more than 1 billion people while emitting no CO_2. This saves approximately 2.5 billion tons of CO_2 per year, with an additional 8 billion tons being emitted from other means of generating power. [3] This makes nuclear technology one of the most promising methods of reducing our global CO_2 emission. At Delft University of Technology, the *Nuclear Energy and Radiation Applications* section conducts research on nuclear reactors for the purpose of producing power.

The Generation IV International Forum (GIF), a research foundation with the aim of evaluating next-generation nuclear reactor technologies, identified and selected six nuclear reactor types for further development. These are intended to offer improved performance, better sustainability, and more inherent safety. The selected designs are the Very-High-Temperature Reactor (VHTR), the Molten Salt Reactor (MSR), the Sodium-cooled, Gas-cooled and Lead-cooled Fast Reactors (SFR, GFR and LFR respectively), and the Supercritical-Water-cooled Reactor (SCWR). [4] These designs are known as the Generation IV reactor types. Reactors currently in operation, such as the BWR and PWR systems, are either Generation II or Generation III designs.

The focus of this thesis lies on the High Performance Light Water Reactor (HPLWR), a variant of the SCWR, proposed by the GIF's European partners. Like conventional BWR and PWR systems, all SCWRs use light water as both coolant and moderator. Unlike these conventional counterparts, however, the SCWR concepts all operate at pressures above the critical point of water. Water at temperatures and pressures above this point ($T_C = 373.9\,°C$, $p_C = 22.06\,\text{MPa}$) is referred to as supercritical. The use of supercritical water as a working fluid allows for a greater range of operating temperatures than in BWR and PWR systems. In addition, SCWR systems can be much more efficient than their previous generation counterparts, offering thermal efficiencies of 44% or higher, compared to 35% for the current reactors. [5] Other benefits include the possibility for smaller reactor containments and smaller turbine systems, lowering the overal cost of the reactor and thereby allowing for cheaper power generation.

1.2. Overview of the High Performance Light Water Reactor

The HPLWR is one of the proposed designs for the SCWR concept. Unique to this design is the configuration of the core, illustrated in figure 1.1. It features three-stage coolant heat-up, with mixing chambers between the stages ensuring a homogeneous temperature distribution in the coolant. This three pass design was first proposed by Schulenberg et al. [6], after finding that heating the fluid up

in one pass would cause the formation of so called hot spots – locally exceeding the temperature limits of the core internals. Mixing the coolant in between the heating zones prevents it from forming hot spots and damaging the core.

The HPLWR is based on the SCWR concept, an overview of which is shown in figure 1.2. The coolant flows into the core at the bottom of the reactor pressure vessel, where it then undergoes the three-stage heating process shown in figure 1.1. The coolant flows upward through the evaporator stage, heating up to about $390\,°\text{C}$. Then, it flows downwards through the first and upwards again through the second superheater stage, where the coolant heats up to about $435\,°\text{C}$ and $500\,°\text{C}$ respectively. During the heating process, the coolant passes the supercritical point and expands significantly. In the natural convection driven design, it then flows upwards through a riser, placed atop the core, not displayed in figure 1.2. The coolant is then led through the turbine system, where the final product, electrical power, is generated. As a final stage, a condenser extracts excess heat, returning the coolant to the desired inlet temperature before sending it back into the core.
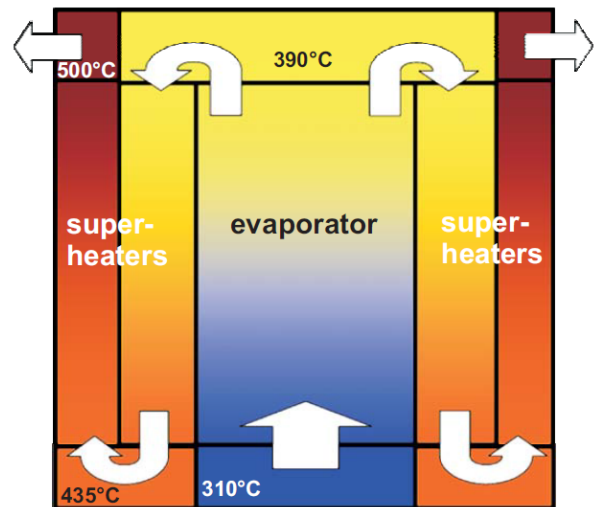

Figure 1.1: Diagram of the coolant flow in the three pass HPLWR core. Mixing chambers are located between every heating stage. [3]

The HPLWR operates at a constant pressure of 25 MPa and at temperatures ranging from $280\,°\text{C}$ at the inlet to $500\,°\text{C}$ at the outlet. This high outlet temperature is possible because it is no longer limited by the vapour-liquid equilibrium, but instead by the material temperature limits. As the water reaches the pseudo-critical temperature ($T_{PC} = 384.9\,°\text{C}$ [1]), the specific heat capacity increases dramatically (see section 1.3). This allows the coolant to carry much greater amounts of heat to the turbines for a certain increase in temperature. As a result of the high outlet temperature, the thermal efficiency of the HPLWR is estimated to be 45%. [3]

In line with the goals adopted by the GIF, the natural convection HPLWR also features improved safety. In a conventional PWR or BWR, the coolant circulation is driven by pumps. Power outages or other technical failures in such pumps can cause them to stop functioning, halting the flow of coolant through the core. In the wrong circumstances, such a failure can result in a core meltdown, with catastrophic consequences. To avoid these situations, ongoing research is being done into systems that do not rely on pumps for the circulation of their coolant.

The HPLWR variant under investigation in this thesis is one of these systems, as it relies on natural convection to drive the coolant circulation. With natural convection driving the coolant flow, the risk of pump failure is eliminated, making the reactor extra safe in emergency situations. Of course, in case of other control issues, pumps are still in place as a back-up device, but they are no longer necessary during operation.

Natural convection arises as a result of extreme density differences within the loop. As is customary for natural circulation driven systems, a riser is placed on top of the core, through which the coolant travels after being heated. A downcomer beside the core allows cooler water to flow downwards. In existing natural convection driven systems, such as the Economic Simplified Boiling Water Reactor (ESBWR), the density difference between liquid water and steam is used to drive the circulation. The colder water in the downcomer is much denser than the steam-water mixture in the riser, causing a gravitational pressure drop. The riser enhances this effect. In the natural convection HPLWR, however, no phase transition takes place. Instead, the design exploits the density difference between water below and above the pseudo-critical point. As the temperature increases from $280\,°\text{C}$ to $500\,°\text{C}$, the density decreases from about 780 kg/m^3 to about 90 kg/m^3 (see figure 1.3). The supercritical water in the riser is much less dense than the subcritical water in the downcomer, and the resulting pressure drop is sufficient to support the circulation
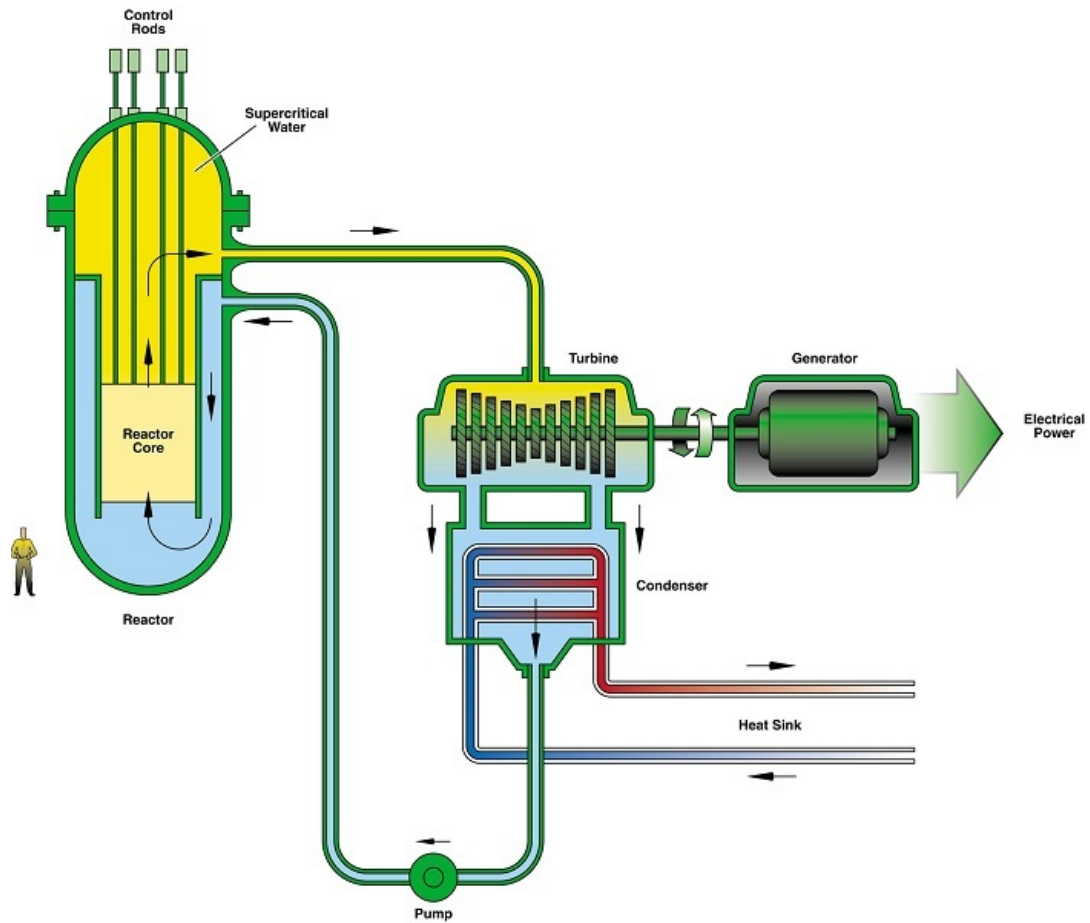
Figure 1.2: Schematic overview of the SCWR concept. In the natural convection driven HPLWR, a riser is present on top of the core. (Not shown in figure) [5]
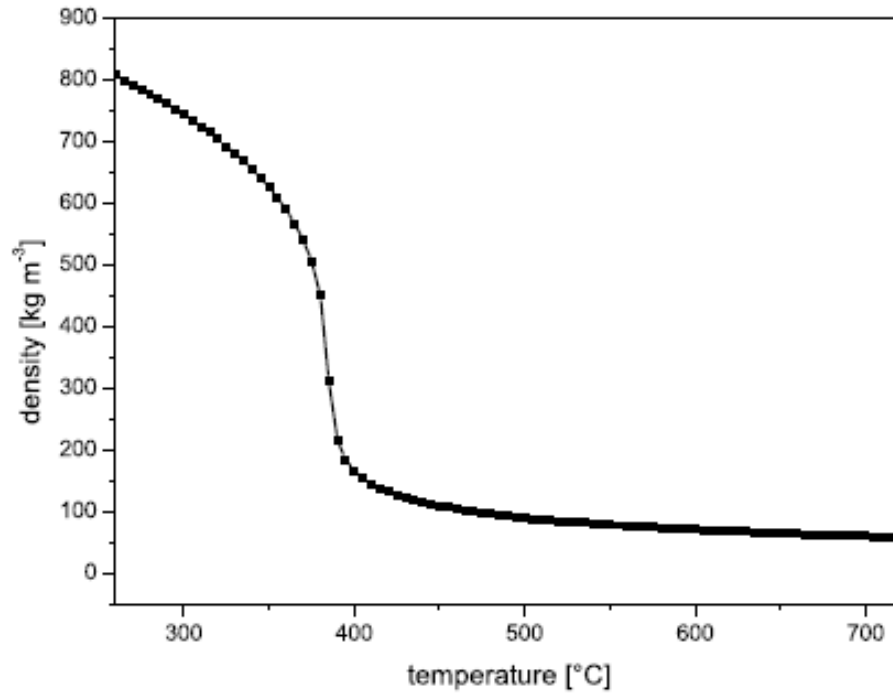
Figure 1.3: Density of water at a pressure of 25 MPa. Between the operating temperatures of the HPLWR (280 °C–500 °C), the density decreases from about 780 kg/m³ to about 90 kg/m³ [3]
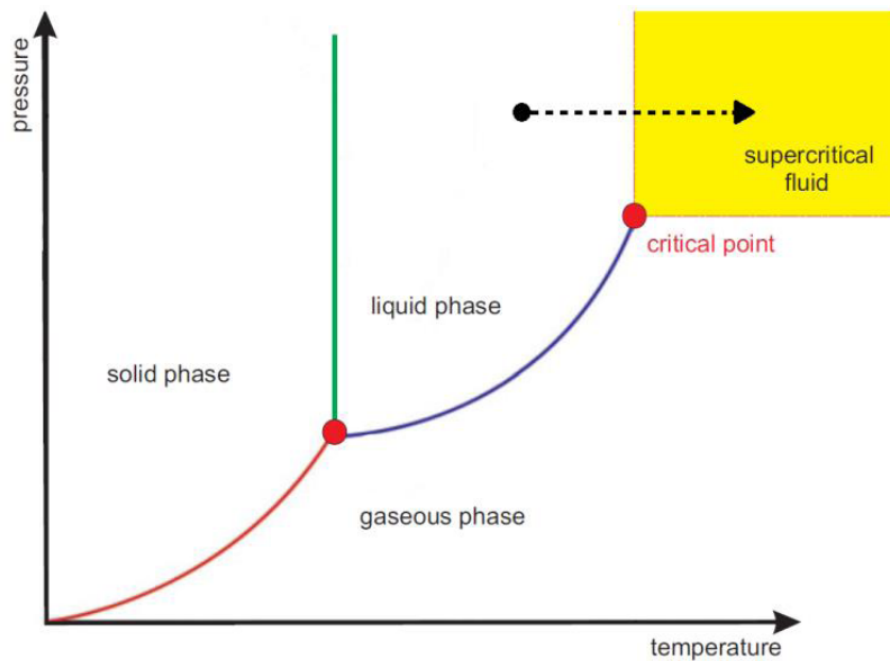
Figure 1.4: Phase diagram of water. The dashed black line shows the operating range of the HPLWR, showing the phase change from liquid to supercritical water as temperature rises. [1]
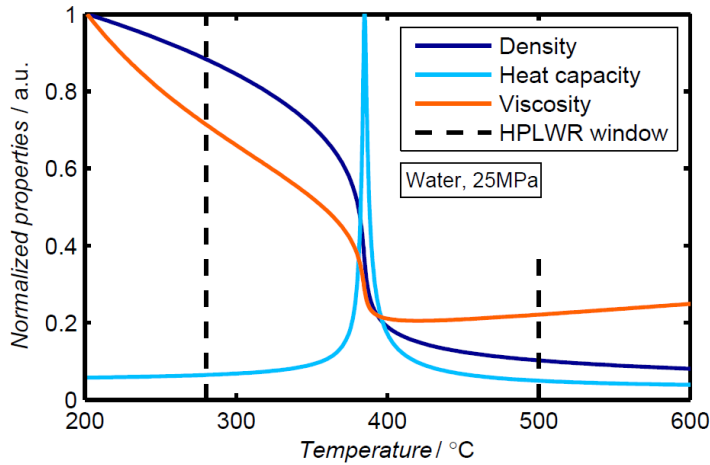
Figure 1.5: Properties of water around the pseudo-critical point. The dashed black lines show the operating range of the HPLWR. [7]

1.3. Supercritical water and the pseudo-critical point

Fluids can exist in various phases, a diagram of which has been provided in figure 1.4 for water. Besides the commonly known solid, liquid, and vapour phases, many other phases exist. One of these is the supercritical phase. Fluids are considered supercritical when both their temperature and their pressure lie above the critical point, which for water lies at $T_C = 373.946\,°C$, $p_C = 22.0640\,MPa$.

Several properties of water, such as the density, viscosity, and specific heat capacity, exhibit highly non-linear behaviour around this point, as shown in figure 1.5. Most notably, the density drops significantly, as figure 1.3 clearly shows. For reasons that will become clear in chapter 2, the pseudo-critical point is used as a reference point in this thesis. Table 1.6 lists various relevant properties of water at the pseudo-critical point. As the water heats up even more, it reaches the pseudo-critical point at $T_{pc} = 384.9\,°C$. This point is defined as the temperature at which water reaches its maximum specific heat capacity.

Figure 1.6: Properties of water at the pseudo-critical point. [8]

Property	Value
T_{pc}	384.9 °C
h_{pc}	$2.1529 \cdot 10^6$ J/kg
ρ_{pc}	316.82 kg/m^3
v_{pc}	$3.1564 \cdot 10^{-3}$ m^{-3}/kg
μ_{pc}	$4.2797 \cdot 10^{-5}$ Pa·s

1.4. Stability

The stability of a system is determined by its response to a perturbation. If the system responds by returning to the configuration it was in before the perturbation occurred, it is considered stable. On the other hand, if the perturbation grows over time, the system is said to be unstable, which may have undesirable effects. Figure 1.7 shows an example of the time development of perturbations in stable and unstable systems. In 2009, Ortega Gómez [3] described various types of instabilities for SCWR type systems. Dynamic instabilities were distinguished from static instabilities, as proposed by Bouré et al. [9]. Static instabilities can be explained from the steady-state equations governing the system, while dynamic instabilities follow from feedback mechanisms in the transient behaviour.

Van Bragt [10] showed that in natural circulation BWR systems, two types of dynamic instabilitie were present. Both these types are generally caused by local density differences and are often referred to as Density Wave Oscillations (DWO). While the BWR exhibits a phase change between liquid and vapour that causes a large density difference within the loop, SCWR systems are considered single-phase. However, since a similar density drop does occur in SCWRs, due to the coolant passing the pseudo-critical point, it is presumed that similar DWO instabilities may be present within the supercritical systems. One of the two identified types of instabilities is the Type-I dynamic instability, which oscillates with low frequencies, and is caused by the gravitational pressure drop in the system. The other type of instability is the Type-II dynamic instability, and is of higher frequency. The Type-II instability is
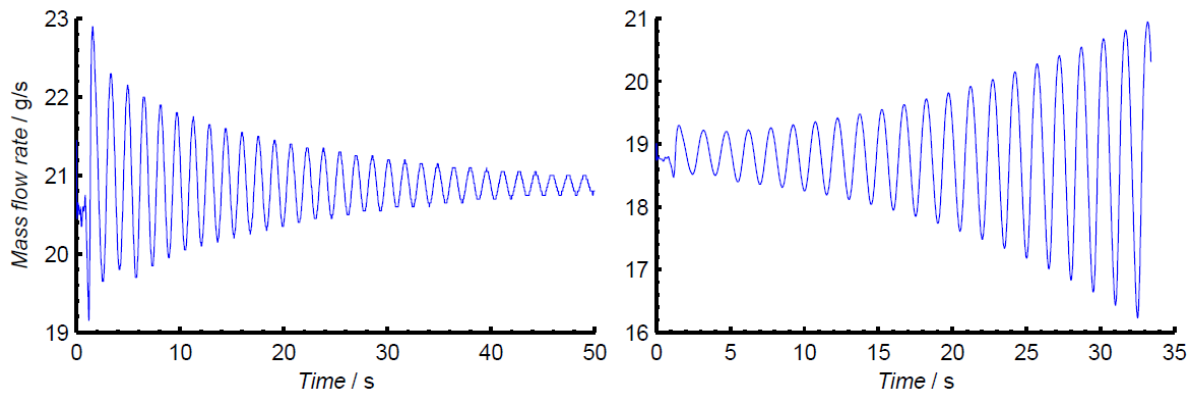
Figure 1.7: Example of the time development of a stable oscillation, on the left, and an unstable oscillation, on the right. [7]
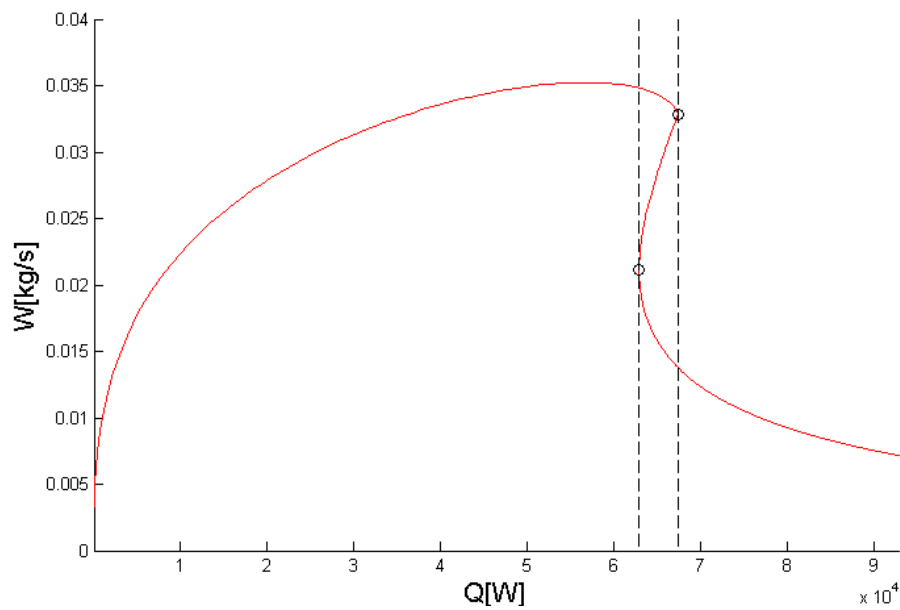
Figure 1.8: Mass flow rate to heating power characteristic of the HPLWR at a fixed inlet temperature. The dashed black lines borders the Ledinegg unstable region.

instead caused by frictional pressure drops [10]. Krijger found the Type-II instabilities in the HPLWR to have frequencies of around 0.1 Hz [1].

The static instabilities in two-phase flows were divided up into three different types by Bouré et. al. [9]; fundamental static instabilities, fundamental relaxation instabilities, and compound relaxation instabilities. Ledinegg instabilities are a type of fundamental static instability, and are the only static instability analysed in this thesis. A Ledinegg instability occurs when the flow undergoes an abrupt, large amplitude change to a new, stable operating condition [9]. In pump-driven systems, these instabilities may occur when the pressure to mass flow rate characteristic of the pump intersects at multiple points with the pressure characteristic of the water loop. In such cases, unstable mass flow rates may suddenly change to another mass flow rate, which may or may not be stable [1, 3]. Since the HPLWR is not driven by a pump but by natural convection, another means of determining Ledinegg unstable conditions must be used. Krijger was able to develop a numerical method of finding Ledinegg instabilities in his model of a supercritical water loop driven by natural convection. It makes use of a property of the mass flow rate to heating power characteristic of the loop. As figure 1.8 shows, more than one mass flow rate is possible for certain heating powers. Therefore, if the heating power is within the range where multiple flow rates are possible, the flow rate may abruptly switch to one of the other possible values — a Ledinegg instability.

1.5. Literature research

The Nuclear Energy and Radiation Applications department of Delft University of Technology has been active in the study of two-phase loops driven by natural circulation for many decades. Among others, Van Bragt analysed the dynamics of BWRs in 1998. The analysis of single-phases systems, however, has not been the subject of studies as much.

In 2004, Lomperski et al. [11] performed experimental research on supercritical CO_2. They used CO_2 because it reaches the supercritical state at lower temperature and pressure than water, while showing similar supercritical characteristics. Lomperski et al. found no flow instabilities, in disagreement with later findings by Chatoorgoon in 2005 [12] and Jain in 2008 [13], who both performed computational analyses.

At Delft University of Technology, an experimental setup for the investigation of the stability characteristics of supercritical fluid loops was built. The Delft Light Water Reactor Facility — DeLight — used Freon R23 as its coolant, which, like CO_2, reaches supercriticality at lower temperature and pressure than water. T'Joen and Rohde [14] performed experimental research on the DeLight facility in 2012, and Kam [15] and Spoelstra [7] analysed the setup numerically in 2011 and 2012 respectively. The numerical research only partially agreed with the DeLight experiment. In 2013, Schenderling [16] augmented Spoelstra's numerical model with thermal inertia, uncovering the significance of the core wall in the stability of the setup. Schenderling also found better agreement with the right hand side of the NSB, showing the same upward trend in his results, as shown in figure 1.9.
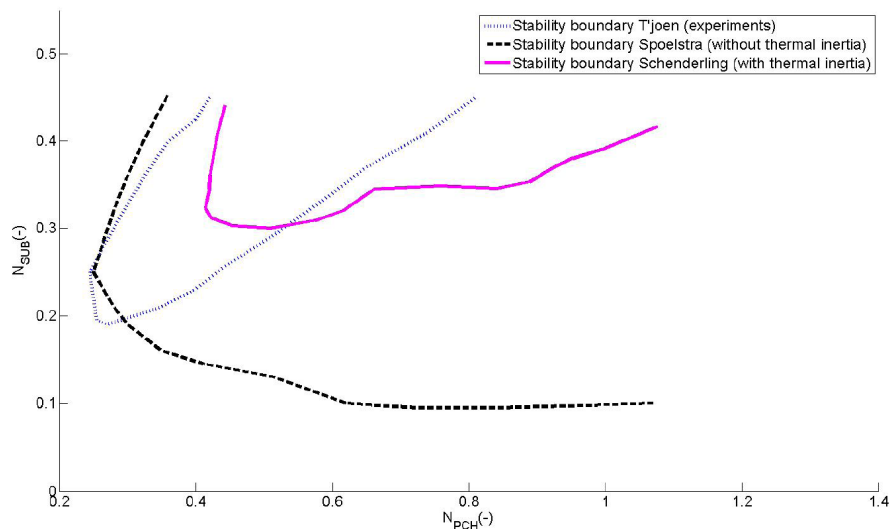
Figure 1.9: Comparison of Spoelstra's and Schenderling's numerical results to the experimental results of T'Joen and Rohde. [16]

In 2009, Ortega Gómez [3] investigated the stability of the HPLWR core under forced circulation, and found no Ledinegg instabilities, flow maldistributions or pressure drop oscillations at steady state under normal operating conditions for the HPLWR. Density wave oscillations were shown to be the most important type of instability present in the HPLWR.

In 2013, Krijger [1] performed a simpler numerical analysis on the natural circulation driven supercritical water loop, breaking the system down into two models with four or five nodes, based on research done by Guido et al. [17]. His analysis did not take core wall thermal inertia or neutronic-thermal-hydraulic coupling into account. Krijger derived heat, mass, and momentum balances for the loop and investigated the stability by linearising these equations, reducing the complicated system to an eigenvalue problem. Krijger established a reference case, and performed a ceteris paribus parametric study on various design decisions of the supercritical water loop. It was found that increasing the length of the riser has a destabilising effect on the system, whereas increasing the volume of the buffer vessel he included in the model improved the system's stability. In 2014, Lippens elaborated on Krijger's work with the inclusion of core wall thermal inertia, also extending the reference case. Lippens found that, while the inclusion of the thermal inertia effect improved stability, the stabilising

effect is reduced as the wall cross-sectional area is increased. In addition, agreement with T'Joen's and Rohde's experiments with Freon R23 improved. Figures 1.10 and 1.11 display stability maps from Krijger's and Lippens' numerical models respectively.
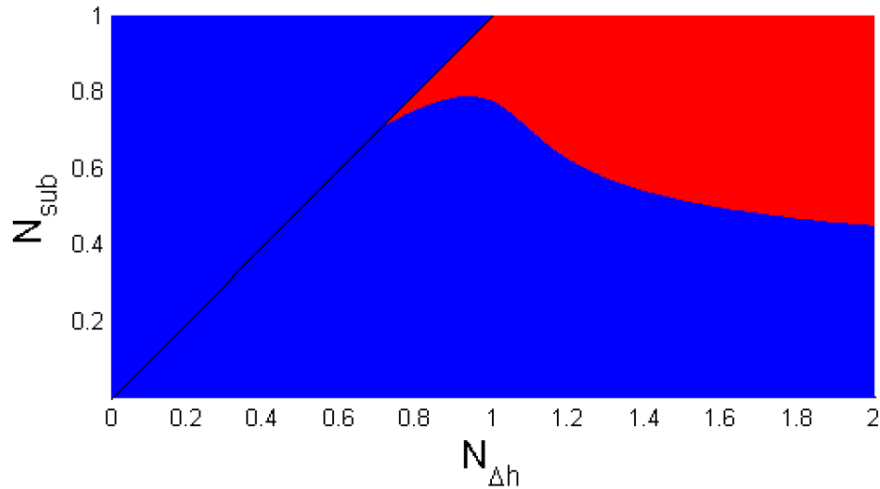
Figure 1.10: Stability map of the reference case established by Krijger [1]. This model does not take into account core wall thermal inertia or neutronic-thermal-hydraulic coupling.
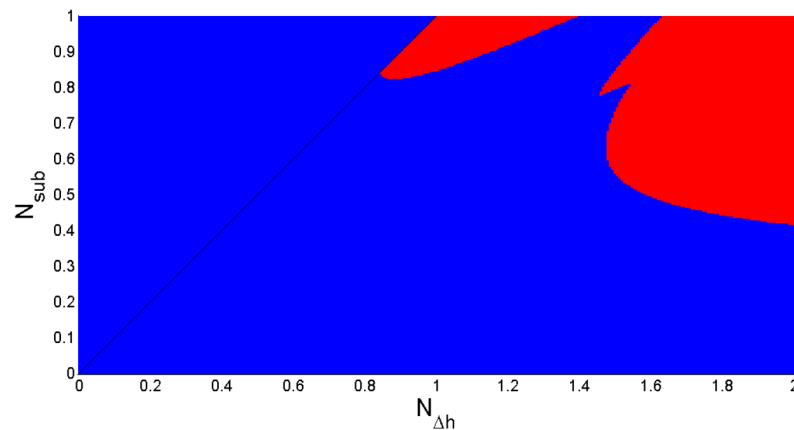
Figure 1.11: Stability map of the reference case established by Lippens [2]. This model does not take into account neutronic-thermal-hydraulic coupling, but does include core wall thermal inertia.

1.6. Thesis outline

This thesis further augments Lippens' extension of Krijger's work through the addition of neutronic-thermal-hydraulic coupling and fuel rod heat transfer modelling. The research follows the same structure as Krijger's and Lippens' work.

In the following chapter, the entirety of the model used in this research will be explained. This includes an overview of the general structure of the model, and several equations used to model various coolant properties from the equation of state. The balance equations governing the system will be presented, and subsequently made dimensionless and linearised. The addition of neutronic-thermal-hydraulic coupling and fuel rod heat transfer is emphasised, while the equations that remain unchanged from Lippens' and Krijger's formulations are not derived separately again. The unchanged equations are presented in their final forms in Appendix B, but for their derivations, we refer the reader to Krijger's and Lippens' original works.

Chapter 3 covers the methods used to analyse the stability from the equations posited in chapter 2, presenting the problem as a generalised eigenvalue problem. Chapter 4 then presents the computational algorithm used to solve the eigenvalue problem, along with further methods for more in-depth analysis of the system's characteristics. These include a resonant frequency analysis and a parametric ceteris paribus study.

Chapter 5 presents the results of the performed analysis. A reference case is first presented, followed by a parametric study on the influence of the coefficients associated with the fuel heat transfer model and the density reactivity feedback as well as the fuel enrichment. Ledinegg instabilities are also briefly touched upon.

Finally, chapter 6 offers conclusions drawn from the stability analyses and some recommendations for further research.

2

Mathematical Model

2.1. Overview

The model used for this thesis is an adaptation of the model used by Lippens [2], who in turn adapted Krijger's model [1]. The basis of the model was developed by Rohde, taking a simplified approach as used by Guido et al. [17] for a boiling water channel. The model Krijger developed simulated a supercritical water loop driven by natural convection, without the inclusion of core wall thermal inertia or neutronic-thermal-hydraulic coupling. Lippens implemented core wall thermal inertia in his adaptation. This thesis extends that model to include neutronics and thermal-hydraulic coupling as well.

As with Guido's model, this model simplifies the core significantly by reducing it to a single channel. This channel has a specified and constant flow cross-sectional area A and hydraulic diameter D_H, and these design parameters remain the same in the riser atop the core as well. After passing through the riser, the coolant travels through a system of turbines and heat exchangers that cool the coolant down to the specified inlet temperature. The entirety of the turbine and heat exchanger system is represented by a single buffer vessel. After the coolant has passed through the buffer vessel, a downcomer leads it back to the core. Whereas the downcomer in the HPLWR is annular, surrounding the core, it too is simplified to a single channel with the same geometry as the riser and core. Since the riser and downcomer are assumed to be perfectly isolated, the buffer vessel is the only part where heat leaves the system.

The geometry of the channel is further shown in figure 2.1. The cladding that surrounds the fuel is referred to as the channel wall, as was done by Lippens in his preceding work.

The model represents each of these parts – core, riser, buffer vessel and downcomer – as nodes, with no further position-dependencies inside. Each node therefore can be characterised by its respective state variables, which may be time-dependent but not position-dependent. Two more nodes that interact with the heat exchange to the coolant, but not the flow of the coolant itself, are also included in the model. These are the core wall node, in which the thermal inertia is modelled, and the fuel node, which accounts for heat transfer from the fuel to the wall.

Because the physical properties of the coolant behave in a highly non-linear fashion around the pseudo-critical point, modelling the core as a single node is no longer a good approximation if that point is reached within the core. For that reason, the core is split up into two nodes, with the
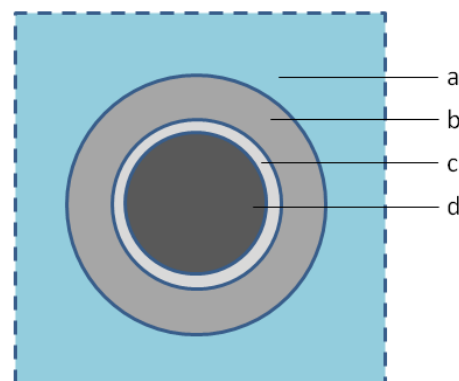

Figure 2.1: Top-down view of the channel geometry. The coolant (a) flows around the fuel rod (b, c and d). b is the channel wall – the cladding surrounding the fuel. The thin layer of gas (c) present in fuel rods is neglected in this research. The fuel itself is labeled d. Not to scale.
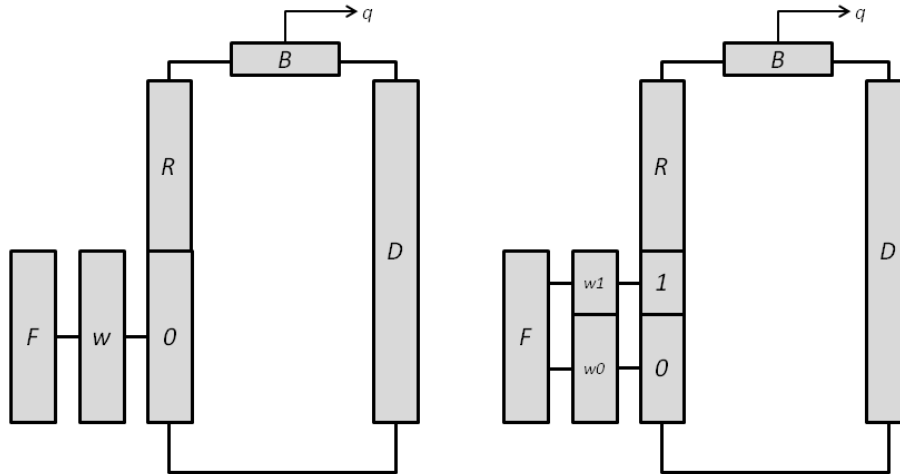
11

Figure 2.2: Overview of the supercritical water loop model. The left figure shows the low-heating model, with the high-heating model to the right. The coolant flows in the clockwise direction. Node labels: *0*: Core node 0; *1*: Core node 1; *w0*: Wall node 0; *w1*: Wall node 1; *F*: Fuel; *R*: Riser; *B*: Buffer vessel; *D*: Downcomer

boundary defined such that it lies at the position where the coolant reaches pseudo-critical enthalpy ($h_{pc} = 2.15 \cdot 10^6$ J/kg). The nodes therefore have variable lengths, that add up to the same core length found in the single node model. If the pseudo-critical point is not reached in the core, the secondary node is unnecessary and the single node model is used. The wall node is split up in the same fashion, so that the lengths of the wall nodes equal the length of their corresponding core nodes. Heat exchange through axial thermal conduction between the two wall nodes is also taken into account. The fuel node is not split up into two parts. Whereas, realistically, the heat generation in the fuel is definitely position dependent, this model is slightly simplified.

The model with a single core node is referred to as the low-heating model, as the coolant is not heated enough to reach pseudo-critical enthalpy. The model in which the coolant does pass the pseudo-critical point is called the high-heating model.

All these nodes put together – six or eight, depending on the model – represent the entire system. They are denoted *0* and *1* for the core nodes, *w0* and *w1* for the corresponding wall nodes, *F* for the the fuel, *R* for the riser, *B* for the buffer vessel, and *D* for the downcomer. The resulting models are graphically represented in figure 2.2. Note that the mixing chambers present in the HPLWR design are not included in the model. Since the state of the coolant is assumed to be position-independent – and therefore perfectly homogeneous – no intermediate homogenisation is necessary.

2.2. Modelling of heat transfer and water properties

2.2.1. Equation of state

If pressure is constant, the equation of state allows us to write the specific volume of the coolant as a direct function of the enthalpy. Because the system does exhibit slight pressure changes, due to gravitational and frictional effects, a simplification is necessary. By neglecting the gravitational and frictional pressure drops for the purpose of the equation of state, a constant system pressure of 25 MPa can be used. This simplification is important, because it allows us to exchange all densities and specific volumes in the balances of sections 2.3 through 2.6 for the enthalpy, thereby eliminating some variables.

Krijger [1] approximated the equation of state using a two-region approach, using pseudo-critical enthalpy as a border between the two. At enthalpies below the pseudo-critical point, the density is assumed to decrease linearly with enthalpy. Above the pseudo-critical point, the specific volume is approximated as a linearly increasing function of enthalpy. Krijger found the gradients of these linear functions to be $C_1 = -4.7877 \cdot 10^{-4}$ and $C_2 = 0.80 \cdot 10^{-8}$ respectively, leading to the following
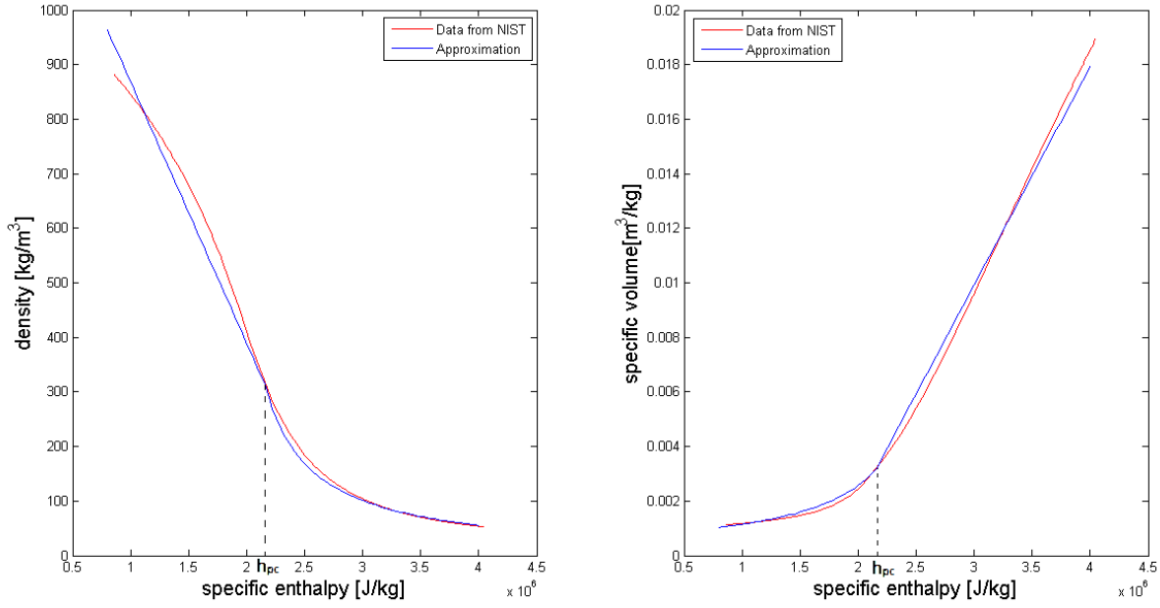
Figure 2.3: Approximation of density (left) and specific volume (right). [1] The red line represents data from NIST. [8]

approximation for the equation of state.

$$v_i = \begin{cases} \frac{1}{\rho_{pc} + C_1(H_i - h_{pc})} & (H_i < h_{pc}) \\ v_{pc} + C_2(H_i - h_{pc}) & (H_i \geq h_{pc}) \end{cases} \tag{2.1}$$

The equation of state is graphically represented in figure 2.3.

2.2.2. Temperature and thermal conductivity

Lippens [2] added approximations for the temperature and thermal conductivity of the coolant as functions of enthalpy. For the temperature approximation, a quadratic approximation was used in both the low and high-enthalpy regions, because of the ease of linearising whilst maintaining the necessary accuracy. Lippens paid specific attention to the continuity of both the approximation and its slope at the pseudo-critical point. The approximation can be expressed by a single equation, shown graphically in figure 2.4,

$$T_i = \alpha_i(H_i - h_{pc})^2 + \frac{1}{c_{p,pc}}(H_i - h_{pc}) + T_{pc} \tag{2.2}$$

in which the subscript i takes a value of either 0 or 1, depending on the region in the enthalpy domain. The coefficients of the quadratic term were found to be $\alpha_0 = -1.1 \cdot 10^{-10}$ and $\alpha_1 = 1.0 \cdot 10^{-10}$ in the low and high-enthalpy regions respectively. The subscript pc denotes the value at the pseudo-critical point. This equation can also be used to calculate the enthalpy at a given temperature.

The thermal conductivity is approximated by a linear function at low enthalpy, and by an exponential function in the high-enthalpy region. Once again, Lippens paid specific attention to ensure that the approximation and its slope are continuous at the pseudo-critical point. Additionally, the coefficients of the linear part were chosen such that the approximation roughly equals the experimental data in a large part of the low-enthalpy region, as shown in figure 2.5.

$$\lambda_f = \begin{cases} -\beta_0 H_0 + \lambda_{f,b,0} & (H_i < h_{pc}) \\ \lambda_z e^{-\beta_1 H_1} + \lambda_{f,b,1} & (H_i \geq h_{pc}) \end{cases} \tag{2.3}$$

This equation uses the following values for the constants, as determined by Lippens:

$$\begin{array}{llll} \beta_0 = & -3.2711 \cdot 10^{-7} & \beta_1 = & 1.3694 \cdot 10^{-6} \\ \lambda_{f,b,0} = & 1.0133 & \lambda_{f,b,1} = & 7.0154 \cdot 10^{-2} & \lambda_z = & 4.5553 \end{array}$$
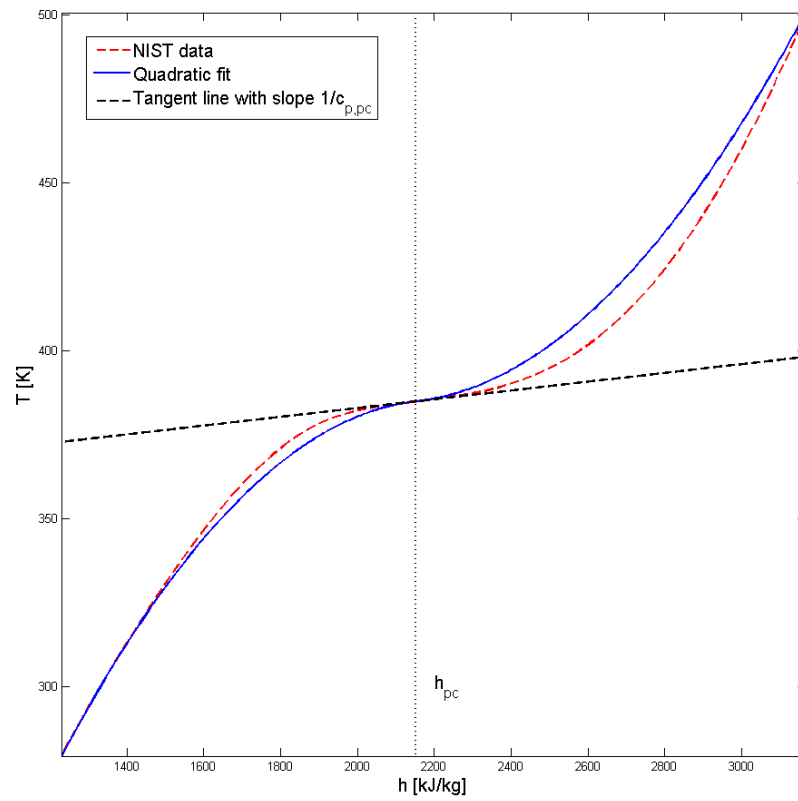
Figure 2.4: Approximation of temperature. The red dotted line represents data from NIST [8]. Figure adapted from Lippens [2].
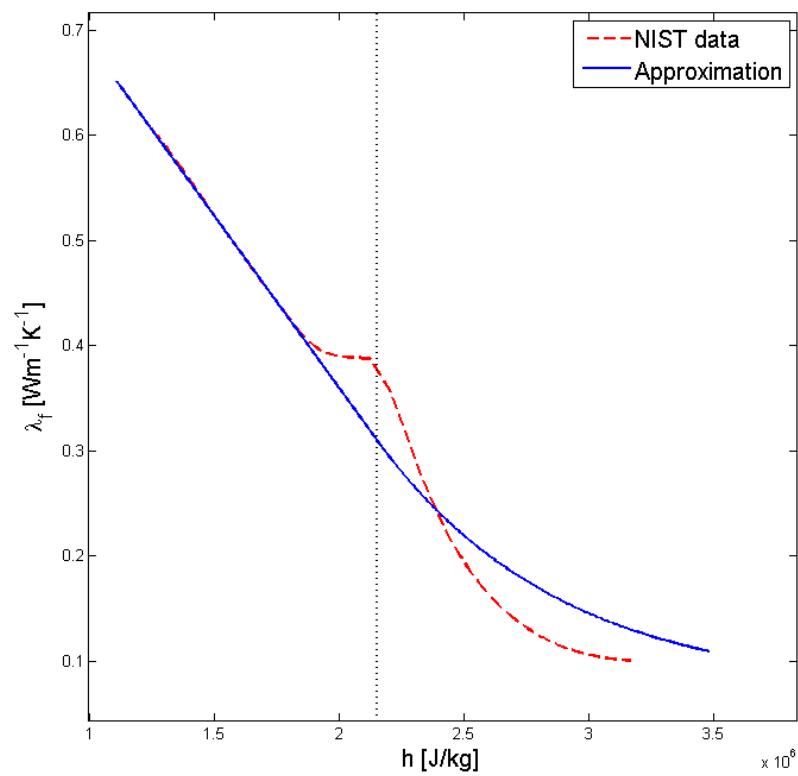
Figure 2.5: Approximation of thermal conductivity. The red dotted line represents data from NIST [8]. Figure adapted from Lippens [2].

2.2.3. Fuel rod heat transfer

The transfer of heat from the fuel to the coolant occurs by conduction through the fuel and the channel wall. In many systems, including the HPLWR, a thin gas layer – the so-called *gap* – is present between the fuel and the channel wall. The heat transfer can therefore be described by three different diffusion equations, which results in a complicated heat transfer function. Taking into account thermal inertia makes this system even more complex. Therefore, three assumptions have been made to simplify the system.

Firstly, the gap has been neglected, for the sake of simplicity. In reality, this gap is a very poor conductor, meaning the temperature of the fuel is higher than the model suggests.

The second assumption is that the heat transfer function, even though it concerns three different materials, is essentially determined by one time constant. Van Bragt [10] made this assumption in his BWR model, and it was used by Spoelstra [7] in his numerical analysis of the HPLWR. This assumption allows us to write the heat transfer function as a first order process, as described in section 2.3.1.

The third assumption is that the heat transfer from the fuel happens entirely within the fuel, and the thermal inertia happens entirely in the wall. This allows us to simplify the heat transfer and thermal inertia to a series of processes instead of two parallel processes. We can justify this simplification by constructing a heat balance across the border between fuel and wall and analysing the consequences.

$$\rho_f c_{p,f} V_f \frac{\mathrm{d}T_f}{\mathrm{d}t} = -\rho_w c_{p,w} V_w \frac{\mathrm{d}T_w}{\mathrm{d}t} + Q''' V_f \tag{2.4}$$

The final term in this equation describes the heating in the fuel, with the other two terms describing the time derivative of the energy content of the fuel and wall respectively. We can rewrite this equation to obtain an expression for the change in temperature of the fuel in response to temperature changes in the wall.

$$\frac{\mathrm{d}T_f}{\mathrm{d}t} = -\frac{\rho_w c_{p,w} V_w}{\rho_f c_{p,f} V_f} \frac{\mathrm{d}T_w}{\mathrm{d}t} + \frac{1}{\rho_f c_{p,f}} Q''' \tag{2.5}$$

Since the densities and heat capacities of the wall and fuel are very similar, but the fuel volume is approximately ten times larger than that of the wall, this is approximately equal to

$$\frac{\mathrm{d}T_f}{\mathrm{d}t} = -\frac{1}{10} \frac{\mathrm{d}T_w}{\mathrm{d}t} + \frac{1}{\rho_f c_{p,f}} Q''' \tag{2.6}$$

showing that the fuel temperature is barely influenced by temperature changes in the wall. It is therefore a reasonable assumption that the fuel heat transfer and wall thermal inertia are two uncoupled processes.

2.3. Balances

Krijger derived a series of transport balance equations that together describe the behaviour of the original 4 or 5-node model. Mass and heat transport balances were derived separately for each node, while the momentum balance was integrated over the entire loop. Lippens subsequently augmented the system with the core wall nodes, explicitly affecting heat transport but not the mass and momentum balances. The mass and momentum balances derived by Krijger and the heat balances derived by Lippens are summarised in Appendix B. By performing some substitutions and discarding variables that do not aid in determining the solution, Krijger was able to reduce the system of equations to a form with equally as many unknown variables. This allows for a unique solution to be found.

2.3.1. Low heating model

In Krijger's model, the heat is supplied directly and constantly to the core. Lippens adjusted this model for the inclusion of thermal inertia by instead supplying the heat directly and constantly to the wall, which then fed the heat into the core by conduction. Lippens' heat balance for the wall node reads:

$$\underline{\text{Ew:}} \qquad \rho_w c_{p,w} A_w L \frac{\mathrm{d}}{\mathrm{d}t} T_w = Q - \frac{Nu_0 \lambda_f}{D_H} P_{in} L(T_w - T_0) \tag{2.7}$$

Here, Ew signifies that this is an Energy balance, concerning the wall node, and that it is one of the governing equations of the system.

This balance is derived from the constant heating term Q adding energy to the wall and the remaining term removing energy by heat transfer to the coolant. Since the heating is no longer constant in the neutronics model, Q must be replaced by a term that accounts for heat transfer from the fuel to the channel wall.

The heat transfer model used is that used by Spoelstra [7] in his numerical analysis of the HPLWR, and can be summarised in one equation. Van Bragt [10] assumed that the transfer function is governed by a single time constant, so that the response to a fluctuation in power of the heat flux to the channel wall can be described as a first order process, with time constant τ:

$$\underline{\text{EF:}} \quad \tau \frac{\partial}{\partial t} \frac{Q_w''(t)}{\overline{Q_w''}} + \frac{Q_w''(t) - \overline{Q_w''}}{\overline{Q_w''}} = \frac{Q(t) - \overline{Q}}{\overline{Q}} \tag{2.8}$$

Here, $\overline{Q_w''}$ and $\overline{Q}$ indicate steady-state values of their respective variables. The time constant is approximated by $\tau = 2$–6 s, as used by Spoelstra for the HPLWR, and originally found by Van der Hagen [18] for the BWR. Q_w'' is the heat flux density from the fuel to the wall, which we multiply by the surface area of the wall to obtain Q_w, the total heat flowing from the fuel to the wall.

We can then replace the variable Q from equation 2.7 with $Q_w(t)$ to simulate heat being fed to the wall from the fuel. This results in the following equation for the heat balance of the wall node:

$$\underline{\text{Ew:}} \quad \rho_w c_{p,w} A_w L \frac{\mathrm{d}}{\mathrm{d}t} T_w = Q_w - \frac{Nu_0 \lambda_f}{D_H} P_{in} L(T_w - T_0) \tag{2.9}$$

To complete this system, we need an expression for $Q(t)$. This can be found by the introduction of neutronics. The volumetric heat generation by nuclear fission is:

$$Q'''(t) = \Sigma_f E_f v_n n(t) \tag{2.10}$$

Obviously, to obtain the total heat production, we just need to multiply by the volume of the fuel: $Q(t) = Q'''(t)V_f$. The macroscopic cross section for thermal fission, Σ_f, is the product of the microscopic fission cross section, σ_f, and the number density of fissile U-235 in the UO$_2$ fuel, $N_{\text{U-235}}$. For U-235, $\sigma_f = 582.6$b. The number density is found as a function of the enrichment ε:

$$M_{\text{U}} = \frac{M_{\text{U-235}} M_{\text{U-238}}}{\varepsilon M_{\text{U-238}} + (1 - \varepsilon) M_{\text{U-235}}} \tag{2.11}$$

$$M_{\text{UO}_2} = M_{\text{U}} + M_{\text{O}_2} \tag{2.12}$$

$$N_{\text{U-235}} = \frac{\rho_{\text{UO}_2} \frac{M_{\text{U}}}{M_{\text{UO}_2}} \varepsilon}{M_{\text{U-235}}} N_A \tag{2.13}$$

$$\Sigma_f = N_{\text{U-235}} \cdot \sigma_f \tag{2.14}$$

Here, N_A is the Avogadro constant, ρ_{UO_2} the density of UO$_2$, and M_X the molar mass of X.

The neutron population $n(t)$ is time-dependent, and is modelled using the six-group point kinetics equations:

$$\underline{\text{n:}} \quad \frac{\mathrm{d}}{\mathrm{d}t} n(t) = \frac{\mathcal{R}(t) - \beta}{\Lambda} n(t) + \sum_{i=1}^{6} \lambda_i C_i(t) \tag{2.15}$$

$$\underline{\text{C}_i:} \quad \frac{\mathrm{d}}{\mathrm{d}t} C_i(t) = \frac{\beta_i}{\Lambda} n(t) - \lambda_i C_i(t), \quad \text{for } i = 1 \dots 6 \tag{2.16}$$

Here, $\mathcal{R}$ is the reactivity — the relative deviation from criticality, β the delayed neutron fraction, Λ the mean generation time, λ_i the precursor decay constant, and C_i the precursor concentration. The values for β_i and λ_i used in this research can be found in appendix C. Equation 2.15 is not linear, and will be linearised in section 2.6 to enable linear analysis. The reactivity is the source of neutronic-thermal-hydraulic coupling, because it is proportional to the coolant density:

$$\mathcal{R} = \alpha_r(\rho_0(t) - \overline{\rho_0}) \tag{2.17}$$

In this equation, $\overline{\rho_0}$ is the steady-state average coolant density in the core. The density reactivity feedback coefficient is defined as $\alpha_r = \frac{\partial \mathcal{R}}{\partial \rho_0}$. Schlagenhaufer et al. [19] found a relation for α_r for the HPLWR:

$$\alpha_r = -1.424 \cdot 10^{-8} \rho_0(t) + 4.236 \cdot 10^{-5} \tag{2.18}$$

In this thesis, the value of ρ_0 was not treated as time-dependent, but instead a constant value was assigned at the start of each calculation. This was done because the fluctuations in coolant density are small enough not to affect the reactivity coefficient significantly, and assuming constant density greatly simplifies the calculations. In addition, treating ρ_0 as time-dependent introduces second-order effects, which would be lost in linearisation. Therefore, this simplification does not greatly affect the accuracy of the model. For the sake of readability, equations 2.18 and 2.17 are not yet substituted into equation 2.15.

2.3.2. High heating model

In the high heating model, the wall is split up into two nodes. Including heat exchange between the wall nodes, Lippens' balances read:

$$\underline{Ew0}: \qquad \rho_w c_{p,w} A_w \frac{\mathrm{d}}{\mathrm{d}t} L_0 T_{w,0} = Q \frac{L_0}{L} - \frac{Nu_0 \lambda_f}{D_H} P_{in} L_0 (T_{w,0} - T_0)$$
$$+ \frac{2\lambda_w}{L} A_w (T_{w,1} - T_{w,0}) \tag{2.19}$$

$$\underline{Ew1}: \qquad \rho_w c_{p,w} A_w \frac{\mathrm{d}}{\mathrm{d}t} L_1 T_{w,1} = Q \frac{L_1}{L} - \frac{Nu_1 \lambda_f}{D_H} P_{in} L_1 (T_{w,1} - T_1)$$
$$- \frac{2\lambda_w}{L} A_w (T_{w,1} - T_{w,0}) \tag{2.20}$$

As in the low heating model, we can simply replace Q by Q_w to obtain the new balances. The balance for the fuel does not change.

In the high heating model, the density of the coolant in node 0 is no longer time-dependent. It instead has a constant average density of $\rho_0 = \frac{1}{2}(\rho_{in} + \rho_{pc})$. The density in node 1 is still time-dependent. This requires us to model the density reactivity feedback slightly differently from the low heating model. The average core density is an average of the densities of the two nodes, weighted by their respective lengths. Using the average core density instead of ρ_0 in equation 2.17 leads to the following derivation for the reactivity:

$$\rho_{core}(t) = \frac{1}{L}(L_0 \rho_0 + L_1 \rho_1(t)) \tag{2.21}$$
$$\mathcal{R} = \alpha_r (\rho_{core}(t) - \overline{\rho_{core}})$$
$$= \alpha_r \left(\frac{1}{L}(L_0 \rho_0 + L_1 \rho_1(t)) - \frac{1}{L}(L_0 \rho_0 + L_1 \overline{\rho_1}) \right)$$
$$= \alpha_r \left(\frac{L_1}{L}(\rho_1(t) - \overline{\rho_1}) \right) \tag{2.22}$$

We then isolate the factor $\frac{L_1}{L}$ and include it in equation 2.25 instead, to more clearly show the dependence of the neutron concentration on the length of the individual core nodes.

The reactivity and reactivity coefficient are now dependent only on ρ_1, and once again are not substituted into equation 2.25. The six precursor equations $\underline{C_i}$ and the fuel heat transfer equation $\underline{EF}$ remain unchanged from the low heating model. This leads to the following equations for the high

heating model:

$$\underline{\text{Ew0}}: \quad \rho_w c_{p,w} A_w \frac{\mathrm{d}}{\mathrm{d}t} L_0 T_{w,0} = Q_w \frac{L_0}{L} - \frac{Nu_0 \lambda_f}{D_H} P_{in} L_0 (T_{w,0} - T_0)$$
$$+ \frac{2\lambda_w}{L} A_w (T_{w,1} - T_{w,0}) \tag{2.23}$$

$$\underline{\text{Ew1}}: \quad \rho_w c_{p,w} A_w \frac{\mathrm{d}}{\mathrm{d}t} L_1 T_{w,1} = Q_w \frac{L_1}{L} - \frac{Nu_1 \lambda_f}{D_H} P_{in} L_1 (T_{w,1} - T_1)$$
$$- \frac{2\lambda_w}{L} A_w (T_{w,1} - T_{w,0}) \tag{2.24}$$

$$\underline{\text{n}}: \quad \frac{\mathrm{d}}{\mathrm{d}t} n(t) = \frac{\frac{L_1}{L} \mathcal{R}(t) - \beta}{\Lambda} n(t) + \sum_{i=1}^{6} \lambda_i C_i(t) \tag{2.25}$$

$$\mathcal{R} = \alpha_r (\rho_1(t) - \overline{\rho_1}) \tag{2.26}$$

$$\alpha_r = -1.424 \cdot 10^{-8} \rho_1(t) + 4.236 \cdot 10^{-5} \tag{2.27}$$

Along with the balances derived by Krijger and Lippens, shown in Appendix B, these balances describe the behaviour of the supercritical water loop model.

2.4. Dimensionless variables

In order to analyse the behaviour of the system in such a way that it is easy to compare it to other system configurations, the entire system of equations is made dimensionless. Krijger and Lippens each introduced dimensionless variables in order to construct the dimensionless balances. For a certain parameter X, its steady-state equivalent is denoted $\overline{X}$, a perturbation as $\check{x}$, and the dimensionless variable $\underline{X}$. The dimensionless variables adopted from Krijger and Lippens are shown in table 2.1. To ease linearisation, Lippens also introduced the adjusted Nusselt number:

$$\widehat{Nu} = Nu\lambda_f^{0.66} \tag{2.28}$$

This change requires a frequently occuring factor, $Nu\lambda_f$, to be replaced by the relation $Nu\lambda_f = \widehat{Nu}\lambda_f^{0.34}$.

Because the adjusted Nusselt number is no longer dimensionless, its dimensionless version is also introduced and included in table 2.1. Several new dimensionless variables were also introduced. These are displayed in table 2.2.

Table 2.1: Dimensionless variables adopted from Krijger (left column) and Lippens (right column).

$\underline{\overline{L_i}} = \frac{\overline{L_i}}{L}$	Length, steady state	$\underline{T_i} = \left(\frac{\lambda_{f,pc}L}{Q}\right) T_i$	Temperature
$\underline{\check{l_i}} = \frac{\check{l_i}}{L}$	Length, perturbation	$\underline{\check{\theta_i}} = \left(\frac{\lambda_{f,pc}L}{Q}\right) \check{\theta_i}$	Temperature, perturbation
$\underline{t} = \frac{t\overline{W}v_{pc}}{AL}$	Time	$\underline{\alpha_i} \left(\frac{Q\lambda_{f,pc}L}{Q}\right) \alpha_i$	Quadratic temperature approximation coefficient
$\underline{\overline{W_i}} = \frac{\overline{W_i}}{\overline{W}} = 1$	Mass flow, steady state	$\underline{c_{p,i}} = \frac{\overline{W}c_{p,i}}{\lambda_{f,pc}L}$	Specific heat capacity
$\underline{\check{w_i}} = \frac{\check{w_i}}{\overline{W}}$	Mass flow, perturbation	$\underline{P_{in}} = \frac{P_{in}}{L}$	Contact perimeter between channel and wall
$\underline{\overline{H_i}} = \frac{\overline{H_i}\overline{W}}{Q}$	Specific enthalpy, steady state	$\underline{\lambda_w} = \frac{\lambda_w A}{\lambda_{f,pc}L^2}$	Wall thermal conductivity
$\underline{\check{h_i}} = \frac{\check{h_i}\overline{W}}{Q}$	Specific enthalpy, perturbation	$\underline{A_w} = \frac{A_w}{A}$	Wall cross-sectional area

Table 2.1: (continued)

$\overline{\underline{\rho_i}} = \overline{\rho}_i v_{pc}$	Density, steady state	$\underline{\lambda_f} = \frac{\lambda_f}{\lambda_{f,pc}}$	Coolant fluid thermal conductivity
$\underline{\check{\rho_i}} = \check{\rho}_i v_{pc}$	Density, perturbation	$\underline{\beta_0} = \frac{\beta_0 Q}{\lambda_{f,pc}\overline{W}}$	Coolant thermal conductivity linear approximation coefficient
$\underline{D_H} = \frac{D_H}{L}$	Hydraulic diameter	$\underline{\beta_1} = \beta_1 \frac{Q}{\overline{W}}$	Coolant thermal conductivity exponential approximation coefficient
$\overline{\underline{V_B}} = \frac{\overline{V}_B}{AL}$	Buffer vessel volume, steady state	$\underline{\widehat{Nu_0}} = \frac{\widehat{Nu_0}}{\lambda_{f,pc}^{0.66}}$	Adjusted Nusselt number

Table 2.2: New dimensionless variables, introduced by the current author.

$\overline{\underline{n}} = \overline{n}AL$	Neutron concentration, steady state	$\overline{\underline{C_i}} = \overline{C}_i AL$	Precursor concentration, steady state
$\underline{\check{n}} = \check{n}AL$	Neutron concentration, perturbation	$\underline{\check{C_i}} = \check{C}_i AL$	Precursor concentration, perturbation
$\overline{\underline{Q_w}} = \frac{\overline{Q}_w}{Q}$	Channel wall heat flux, steady state	$\underline{\lambda_i} = \lambda_i \frac{AL}{\overline{W}v_{pc}}$	Decay constant
$\underline{\check{q}_w} = \frac{\check{q}_w}{Q}$	Channel wall heat flux, perturbation	$\underline{\Lambda} = \Lambda \frac{\overline{W}v_{pc}}{AL}$	Neutron generation time
$\underline{\alpha_r} = \alpha_r \rho_{pc}$	Density reactivity feedback coefficient	$\underline{\Sigma_f} = \Sigma_f L$	Macroscopic neutron cross section
$\underline{v_n} = v_n \frac{AL^2}{\overline{W}v_{pc}}$	Neutron velocity	$\underline{E_f} = E_f \frac{v_{pc}}{ALh_{pc}}$	Energy released per fission event
$\underline{\tau} = \tau \frac{\overline{W}v_{pc}}{AL}$	Fuel heat transfer time constant	$\underline{V_f} = \frac{V_f}{AL}$	Fuel volume

2.5. Dimensionless balances

All new balances and equations need to be made dimensionless, and will be displayed in the following two sections for the low and high heating models respectively. The dimensionless balances derived by Krijger and Lippens can be found in Appendices B.3 and B.4. Any balance not mentioned in the following two sections is unchanged from Lippens' thesis and is adopted as such. Since Lippens adopted several balances from Krijger's thesis without modification, many balances in this thesis do not differ from those derived by Krijger.

2.5.1. Low heating model

The dimensionless balances for the low heating model are presented in this section. They are obtained simply by substituting variables by their dimensionless counterparts. In addition, the temperature T_0 in the $\underline{Ew}$ balance is substituted by the quadratic approximation of section 2.2.2. (See Lippens [2]). The expression for $Q(t)$, equation 2.10, is also substituted into the $\underline{EF}$ balance. This results in the following dimensionless balance equations:

$$\underline{Ew}: \quad \rho_w c_{p,w} A_w \frac{\mathrm{d}}{\mathrm{d}\underline{t}}\underline{T_w} = \underline{Q_w} - \widehat{Nu_0}\lambda_{f0}^{0.34}\frac{\underline{P_{in}}}{\underline{D_H}}\left(\underline{T_w} - \underline{T_{pc}}\cdots\right.$$

$$\left.\cdots - \underline{\alpha_0}\left(\underline{H_0} - h_{pc}\right)^2 - \frac{1}{\underline{c_{p,pc}}}\left(\underline{H_0} - h_{pc}\right)\right) \tag{2.29}$$

$$\underline{EF}: \quad \underline{\tau}\frac{\partial}{\partial\underline{t}}\underline{Q_w''} = \Sigma_f E_f V_f v_n \underline{n} - \underline{Q_w''} \tag{2.30}$$

$$\underline{n}: \quad \frac{\mathrm{d}}{\mathrm{d}\underline{t}}\underline{n} = \frac{\mathcal{R} - \beta}{\underline{\Lambda}}\underline{n} + \sum_{i=1}^{6}\lambda_i C_i \tag{2.31}$$

$$\underline{C_i}: \quad \frac{\mathrm{d}}{\mathrm{d}\underline{t}}\underline{C_i} = \frac{\beta_i}{\underline{\Lambda}}\underline{n} - \underline{\lambda_i C_i} \tag{2.32}$$

2.5.2. High heating model

The same process as applied in the previous section is used for the high heating model. Once again, the equations $\underline{C_i}$ and $\underline{EF}$ do not differ from those of the low heating model. The resulting dimensionless equations are as follows:

$$\underline{Ew0}: \quad \rho_w c_{p,w} A_w\left(1 - \underline{L_1}\right)\frac{\mathrm{d}}{\mathrm{d}\underline{t}}\underline{T_{w,0}} - \rho_w c_{p,w} A_w T_{w,0}\frac{\mathrm{d}}{\mathrm{d}\underline{t}}\underline{L_1} = \underline{Q_w} - \underline{L_1}\cdots$$

$$\cdots - \widehat{Nu_0}\lambda_{f0}^{0.34}\frac{\underline{P_{in}}\left(1 - \underline{L_1}\right)}{\underline{D_H}}\left(\underline{T_{w,0}} - \underline{T_{pc}} - \underline{\alpha_0}\left(\underline{H_0} - h_{pc}\right)^2\cdots\right.$$

$$\left.\cdots - \frac{1}{\underline{c_{p,pc}}}\left(\underline{H_0} - h_{pc}\right)\right) + 2\underline{\lambda_w}A_w\left(\underline{T_{w,1}} - \underline{T_{w,0}}\right) \tag{2.33}$$

$$\underline{Ew1}: \quad \rho_w c_{p,w} A_w\underline{L_1}\frac{\mathrm{d}}{\mathrm{d}\underline{t}}\underline{T_{w,1}} + \rho_w c_{p,w} A_w T_{w,1}\frac{\mathrm{d}}{\mathrm{d}\underline{t}}\underline{L_1} = \underline{Q_w} + \underline{L_1}\cdots$$

$$\cdots - \widehat{Nu_1}\lambda_{f1}^{0.34}\frac{\underline{P_{in}L_1}}{\underline{D_H}}\left(\underline{T_{w,1}} - \underline{T_{pc}} - \underline{\alpha_1}\left(\underline{H_1} - h_{pc}\right)^2\cdots\right.$$

$$\left.\cdots - \frac{1}{\underline{c_{p,pc}}}\left(\underline{H_1} - h_{pc}\right)\right) - 2\underline{\lambda_w}A_w\left(\underline{T_{w,1}} - \underline{T_{w,0}}\right) \tag{2.34}$$

$$\underline{n}: \quad \frac{\mathrm{d}}{\mathrm{d}\underline{t}}\underline{n} = \frac{\underline{L_1}\mathcal{R} - \beta}{\underline{\Lambda}}\underline{n} + \sum_{i=1}^{6}\lambda_i C_i \tag{2.35}$$

2.6. Linearised balances

2.6.1. Linearisation

In this thesis, the model is solved using linear methods. In order to use linear solving techniques, the model equations must first be linearised. This is done by expressing each time-dependent variable as the sum of its steady-state value and a small perturbation:

$$X = \overline{X} + \check{x} \tag{2.36}$$

Products of perturbations with eachother or with time derivatives of other perturbations are then discarded, leaving only linear terms. Because we require the perturbations to be small, this simplification does not drastically affect the accuracy of the model. After all, the products of perturbations will be even smaller. Finally, the steady-state solutions are subtracted from both sides of the equations, leaving a system of n first-order linear differential equations with n variables. The following is an example of this linearisation process:

$$\begin{aligned} XY &= \left(\overline{X} + \check{x}\right)\left(\overline{Y} + \check{y}\right) \\ &= \overline{XY} + \overline{X}\check{y} + \overline{Y}\check{x} + \check{x}\check{y} \\ &\approx \overline{XY} + \overline{X}\check{y} + \overline{Y}\check{x} \end{aligned} \tag{2.37}$$

The $\overline{XY}$ term is then subtracted. This method of linearisation also allows us to write equation 2.17 as

$$\mathcal{R} = \alpha_r \check{\rho}_0 \tag{2.38}$$

and equation 2.8 as

$$\tau \frac{\partial}{\partial t}\check{q}_w - \check{q}_w = \check{q} \tag{2.39}$$

Krijger and Lippens also provided linearisations of the properties modeled through the equation of state through a first-order Taylor expansion. With ρ_0 linearised, we can easily substitute equation 2.38 into our n balance. The linearisations of all equations added or changed in this thesis are provided in the following two sections for the low and high heating models respectively. In some of these equations, the dimensionless pseudo phase change number appears, which will be further explained in section 3.2. It is defined as

$$N_{\Delta h} \equiv \frac{Q}{\overline{W}h_{pc}}$$

The balances that remain unchanged from Lippens' work can be found in Appendices B.5 and B.6.

2.6.2. Low heating model

The linearised balances for the low heating model read:

$$\underline{\text{Ew:}} \qquad \rho_w c_{p,w} A_w \frac{\mathrm{d}}{\mathrm{d}\underline{t}}\check{\theta}_w = \check{q}_w - \widehat{Nu_0}\overline{\lambda}_{f0}^{-0.34}\frac{P_{in}}{D_H}\check{\theta}_w \cdots$$

$$\cdots + \frac{1}{2}\widehat{Nu_0}\frac{P_{in}}{D_H}\left(\overline{\lambda}_{f0}^{-0.34}\left(2\alpha_0\left(H_0 - h_{pc}\right) + \frac{1}{c_{p,pc}}\right)\cdots\right.$$

$$\cdots - 0.34\overline{\lambda}_{f0}^{-0.66}\left(\overline{T}_w - \overline{T}_0\right)\beta_0\right)\check{h}_{out} \tag{2.40}$$

$$\underline{\text{EF:}} \qquad \tau\frac{\partial}{\partial\underline{t}}\check{q}_w = \Sigma_f E_f V_f v_n \check{n} - \check{q}_w \tag{2.41}$$

$$\underline{\text{n:}} \qquad \frac{\mathrm{d}}{\mathrm{d}\underline{t}}\check{n} = \frac{\alpha_r \overline{n} C_1 N_{\Delta h} h_{pc} v_{pc}\check{h}_0 - \beta\check{n}}{\Lambda} + \sum_{i=1}^{6}\lambda_i\check{C}_i \tag{2.42}$$

$$\underline{\text{C}_i:} \qquad \frac{\mathrm{d}}{\mathrm{d}\underline{t}}\check{C}_i = \frac{\beta_i}{\Lambda}\check{n} - \lambda_i\check{C}_i \tag{2.43}$$

2.6.3. High heating model

The linearised balances for the high heating model read:

$$
\underline{\text{Ew0:}} \qquad \rho_w c_{p,w} A_w \overline{L_0} \frac{\mathrm{d}}{\mathrm{d}\underline{t}} \underline{\check{\theta}_{w,0}} - \rho_w c_{p,w} A_w \overline{T}_{w,0} \frac{\mathrm{d}}{\mathrm{d}\underline{t}} \underline{\check{l}_1} =
$$

$$
\left(1 - \underline{L_1}\right) \underline{\check{q}_w} + \left(\widehat{Nu_0} \overline{\lambda}_{f0}^{-0.34} \frac{P_{in}}{\underline{D_H}} \left(\overline{T}_{w,0} - \underline{T_0} \right) - 1 \right) \underline{\check{l}_1} \cdots
$$

$$
\cdots - \left(\widehat{Nu_0} \overline{\lambda}_{f0}^{-0.34} \frac{P_{in}\overline{L_0}}{\underline{D_H}} + 2\underline{\lambda_w A_w} \right) \underline{\check{\theta}_{w,0}} + 2\underline{\lambda_w A_w \check{\theta}_{w,1}} \tag{2.44}
$$

$$
\underline{\text{Ew1:}} \qquad \rho_w c_{p,w} A_w \overline{L_1} \frac{\mathrm{d}}{\mathrm{d}\underline{t}} \underline{\check{\theta}_{w,1}} + \rho_w c_{p,w} A_w \overline{T}_{w,1} \frac{\mathrm{d}}{\mathrm{d}\underline{t}} \underline{\check{l}_1} =
$$

$$
\underline{L_1 \check{q}_w} + \left(1 - \widehat{Nu_1} \overline{\lambda}_{f1}^{-0.34} \frac{P_{in}}{\underline{D_H}} \left(\overline{T}_{w,1} - \underline{T_1} \right) \right) \underline{\check{l}_1} \cdots
$$

$$
\cdots + \widehat{Nu_1} \frac{P_{in}\overline{L_1}}{\underline{D_H}} \left(\left(2\underline{\alpha_1} \left(\overline{H_1} - h_{pc} \right) + \frac{1}{\underline{c_{p,pc}}} \right) \overline{\lambda}_{f1}^{-0.34} \cdots \right.
$$

$$
\left. \cdots + 0.34 \left(\overline{T}_{w,1} - \underline{T_1} \right) \overline{\lambda}_{f1}^{-0.66} \beta_1 \lambda_z e^{-\beta_1 \overline{H_1}} \right) \underline{\check{h}_1} \cdots
$$

$$
\cdots + 2\underline{\lambda_w A_w \check{\theta}_{w,0}} - \left(\widehat{Nu_1} \overline{\lambda}_{f1}^{-0.34} \frac{P_{in}\overline{L_1}}{\underline{D_H}} + 2\underline{\lambda_w A_w} \right) \underline{\check{\theta}_{w,1}} \tag{2.45}
$$

$$
\underline{\text{n:}} \qquad \frac{\mathrm{d}}{\mathrm{d}\underline{t}} \underline{\check{n}} = -\frac{C_2 N_{\Delta h} h_{pc} \alpha_r \overline{L_1} \overline{n}}{v_{pc} \Lambda \overline{v}_1^2} \underline{\check{h}_1} - \frac{\beta}{\underline{\Lambda}} \underline{\check{n}} + \sum_{i=1}^{6} \lambda_i \underline{\check{C}_i} \tag{2.46}
$$

3

Method of Stability Investigation

To determine the stability of the system under certain operating conditions, a solution must be found to the set of equations governing the system. The main reason for linearising these equations is the ease of solving them. This chapter will describe how the solutions are found and what parts are of interest. In addition, a way of determining and enforcing the operating conditions is presented.

3.1. Matrix equation

In chapter 2, we presented two different sets of equations for which solutions must be found. The low heating model consists of 13 equations with 13 variables. In the high heating model, there are 16 equations with 16 variables. Since all equations are linear, first order differential equations, we can write the sets of equations as:

$$A \frac{\mathrm{d}}{\mathrm{d}t} \vec{x} = B \vec{x} \tag{3.1}$$

Here, $\vec{x}$ is a column vector containing the perturbed variables, B is a matrix containing the coefficients of the perturbed variables, and A contains the coefficients of the perturbed variables' time derivatives. The matrices A and B are both square and equal in size; 13×13 in the low heating model and 16×16 in the high heating model. Because of their sizes, the matrices A and B are not displayed here, but they can be found in Appendix A. Each linearised balance populates a row of the matrices, and each column represents one of the perturbed variables.

The matrix equation has solutions of the form $\vec{x} = \vec{v}e^{\lambda t}$, in which the vector $\vec{v}$ contains the amplitude and phase shift of the inital perturbation. The time-evolution of this solution depends on λ. For negative values of λ, the perturbation will decay exponentially with time and die out. If λ is positive, the perturbation will grow exponentially over time. Such exponential growth can cause perturbations with large amplitudes in the system, potentially with dramatic consequences. These situations are *unstable*.

It is evident, then, that λ is the only variable of interest for determining the stability. Since there is no restriction that says otherwise, λ can be complex. The real part of λ determines the stability of the system, whereas the imaginary part determines the oscillation frequency of the related perturbation. Multiple instabilities may be present at any given time, but the instability with the largest real part of λ will dominate eventually. Therefore, it suffices to look at the imaginary part of the largest real λ.

λ can be decomposed as $\lambda = a + \omega i$, in which a is the amplitude of the instability, and ω is its resonance frequency.

To find λ, equation 3.1 is rewritten by substituting the proposed solution into the equation and then dividing by $e^{\lambda t}$:

$$A \lambda \vec{v} = B \vec{v} \tag{3.2}$$

This equation cannot be solved by simply multiplying by A^{-1}, because A is a singular matrix – it has no inverse. We have encountered a generalised eigenvalue problem, which can be solved by finding the solutions to $\det(B - A\lambda) = 0$. These solutions are determined computationally, and chapter 4 will expand on that further. The eigenvalues are computed for each operating point, resulting in a map of stable and unstable regions.

3.2. Operating points

To evaluate the stability characteristics of the system at every possible set of operating conditions, we must make a convenient choice in how to define these conditions. Throughout literature, many dimensionless numbers are used as measures for the heating power, inlet temperature and mean flow rate, the three operating conditions considered. Krijger chose to use slightly modified versions of the dimensionless numbers used by T'Joen and Rohde [14], which Lippens adopted for his analysis. The same measures are used in this research as well.

Section 2.6 already briefly introduced the pseudo phase change number,

$$N_{\Delta h} \equiv \frac{Q}{\overline{W} h_{pc}} \tag{3.3}$$

It is a measure of enthalpy increase in the core section. Since the HPLWR is driven by natural convection instead of pumps, the mass flow $\overline{W}$ is determined by the heating power Q and the inlet temperature. The mass flow and heating power will both always be positive, so the pseudo phase change number is too.

The subcooling number is a measure of inlet enthalpy and thereby inlet temperature. It is defined as

$$N_{sub} \equiv 1 - \frac{H_{in}}{h_{pc}} \tag{3.4}$$

As the temperature – and therefore the enthalpy – increases, the subcooling number decreases. Although it is not necessarily the case, it is assumed that the inlet enthalpy does not exceed pseudo-critical enthalpy. Therefore, the subcooling number cannot be negative. The subcooling number can also never exceed unity, because enthalpy cannot take on negative values.

4

Computational Implementation

4.1. Considerations

The computational implementation of the problem described in the previous chapters is done by modifying a MATLAB programme, developed by Krijger and Lippens. The basic structure of the programme was written by Krijger, who developed it for evaluating the supercritical water loop; Lippens augmented the code to account for core wall thermal inertia.

While writing the original code, Krijger made sure the code was comprehensible and easily readable. Lippens endeavoured to maintain this readability, so that the code could be easily adapted for further research. For this reason, the adjustibility of input parameters was also considered. Because the computational power required to calculate the requested solutions is fairly minor, efficiency was not greatly emphasised in the code. [1]

The modifications to the code done by this author account for neutronic-thermal-hydraulic coupling as well as heat transfer from the fuel to the coolant. For this purpose, various new input parameters are introduced, which describe the properties of the fuel as well as the neutronics. Examples are the fuel heat transfer time constant, the fuel enrichment and the density reactivity feedback coefficient. The coefficient matrices are extended to include the equations governing neutronics and fuel rod heat transfer, and the calculations of dimensionless variables for these equations are added.

In both the low and high heating models, setting the density reactivity feedback coefficient α_r to zero returns the model to the case evaluated by Lippens. This is the case, because for $\alpha_r = 0$, equations 2.15 and 2.16 decouple from the rest of the system and no longer influence the dynamics of the system. This case is used as a benchmark.

Further considerations are made to ensure the model adheres to certain constraints: The coolant enthalpy may never exceed pseudo-critical enthalpy in the low heating model, the length of core node 1 – see figure 2.2 – must be greater than or equal to zero in the high heating model, and the steady state mass flow must be real-valued. Lippens implemented various warnings in case these requirements are violated.

The following section discusses further details on the algorithm.

4.2. Algorithm

4.2.1. Basic structure

The algorithm follows the same basic structure as Lippens' and Krijger's code, displayed graphically in figure 4.1. First of all, the workspace is cleared. Then, a number of input parameters are specified. These parameters describe the domain and resolution of the instability map and the accuracy of the steady-state calculations, but also the geometry of the loop, the fluid properties of the coolant, and the neutronic properties of the fuel. The ranges of $N_{\Delta h}$ and N_{sub} are divided into N linearly spaced points, and an $N \times N$ stability matrix of zeros is created. After the input parameters are specified, the programme runs through two nested FOR-loops – one for every value of N_{sub}, the second for every value of $N_{\Delta h}$. Krijger showed that if $N_{\Delta h} \leq N_{sub}$, the high heating model is invalid, so the low heating

model is used. The high heating model is used for $N_{\Delta h} \geq N_{sub}$. The programme uses an IF-statement to distinguish between the two and loops the appropriate code for every point.

In these loops, the first step is the calculation of operational characteristics that are independent of the flow. After this, a WHILE-loop is initiated to iteratively calculate the steady-state flow values to the desired accuracy. Subsequently, all flow-dependent variables are calculated, and all values are normalised – made dimensionless. This is enough information to build the coefficient matrices for the eigenvalue problem, which can then be solved. It is determined whether the chosen point in the N_{sub} - $N_{\Delta h}$ plane is stable, and if so, a value of 1 is assigned to that point in the stability matrix. The programme returns to the top of the FOR-loop and continues with the next point, until all points are evaluated.

After all points are done, the instability matrix is complete and can be converted to a colour map. The stable points are coloured blue, while the unstable points are displayed in red. Several modifications to the code, discussed in section 4.3, allow for the output of resonance frequency maps, Ledinegg instability maps, and neutral stability boundaries for easy comparison of different input parameters.
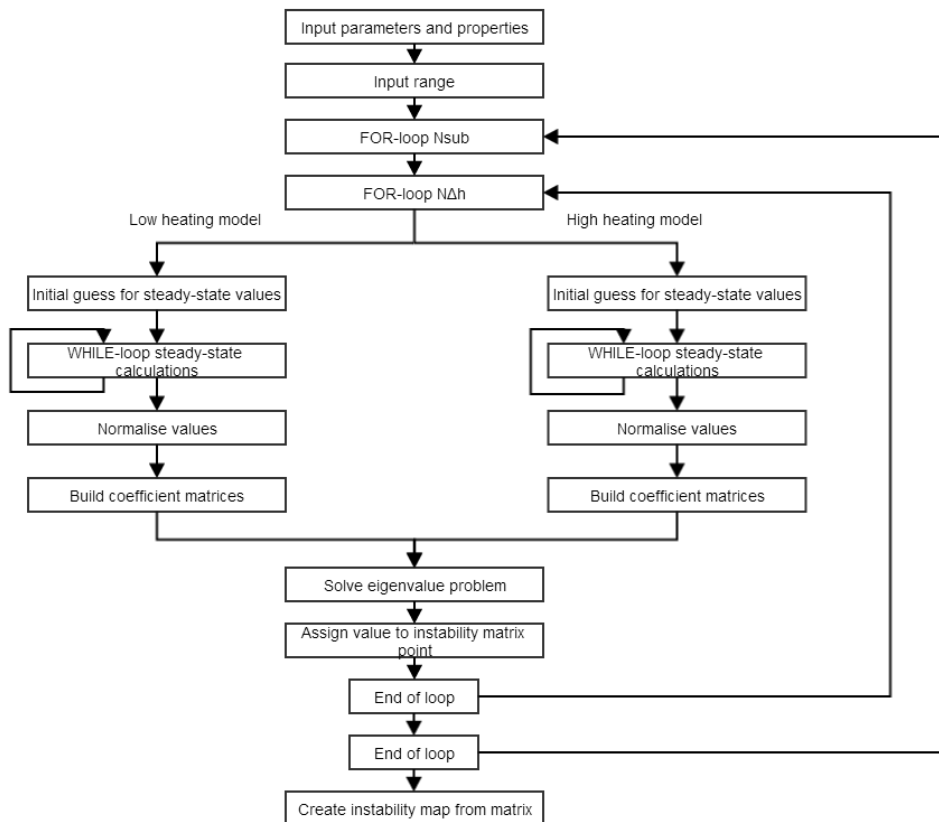
Figure 4.1: Flow chart of the general structure of the algorithm used to generate stability maps.

4.2.2. Determining steady-state values

Several steady-state variables can be calculated directly in the FOR-loops, without using iterative calculations. In Krijger's model, all operational characteristics except the Reynolds number and mass flow rate were defined directly. In the model Lippens developed, direct definitions can only be used for the inlet enthalpy and inlet specific volume. All other operational characteristics are heavily interdependent, and must be evaluated iteratively.

The WHILE-loop, in which these iterative calculations are performed, is executed until the relative difference in mass flow rates between the last two iterations is smaller than `dwres`, an input variable used solely for this resolution. It allows the user to choose for either a more precise or a faster calculation. For precise calculations, `dwres` = 10^{-12} is a suitable value; for faster calculations, `dwres` = 10^{-9} still gives good results. If the input parameters are chosen such that the mass flow rate does not converge, the loop terminates after reaching a fixed number of iterations, `itlim`, to be set by the

user. If the iteration limit is exceeded, a warning is displayed. The default value is `itlim` = 1000.

4.2.3. Eigenvalue problem

Once the steady-state values have been determined, the coefficient matrices A and B can be built. The matrix equation 3.1 governing the system is then solved by use of MATLAB's `eig` function. To solve a generalised eigenvalue problem where matrix A is singular, it is necessary to use the QZ algorithm, also known as the generalised Schur decomposition. The `eig` function employs this algorithm to solve $\det(B - A\lambda) = 0$ and returns the eigenvalues. [20]

A generalised eigenvalue problem with $n \times n$ matrices has up to n eigenvalues associated with it, but not necessarily that many. Koren [21] found that, despite this, MATLAB always returns exactly n values. Some of these values will be infinite, and, as such, are not eigenvalues of the system. In the stability analysis, these infinite eigenvalues are therefore disregarded.

MATLAB may also sometimes return extremely small eigenvalues, often smaller than 10^{-12}. These are likely due to floating point rounding errors, and can therefore safely be disregarded as well.

After these values, that do not contribute, have been filtered out, the sign of the remaining eigenvalues is analysed. If any of the eigenvalues has a positive real part, the operating point in the N_{sub} - $N_{\Delta h}$ plane associated with it is considered dynamically unstable. If all eigenvalues have negative real parts, the point is considered dynamically stable, and the point in the stability matrix is assigned a value of 1.

4.3. Additional analyses

Krijger included in his code several additions that allow for investigation in more detail of the stability characteristics. These modifications to the code are described in the following three sections.

4.3.1. Ledinegg instabilities

In studying the mass flow rate versus heating power characteristic, Krijger found that under certain conditions, Ledinegg instabilities may occur. As described in section 1.4, Ledinegg instabilities may occur when the slope of this characteristic swaps sign at least three times. Figure 4.2 illustrates this. It shows that there are values of the power for which more than a single mass flow rate is possible. Krijger used this definition to determine which points in the instability map were Ledinegg unstable, and included code to overlay a map of Ledinegg unstable points on the dynamic instability map.
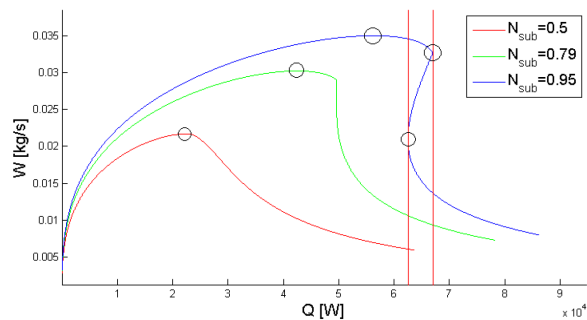
Figure 4.2: Mass flow rate versus heating power characteristic for various subcooling numbers. Sign swaps are indicated by black circles. The vertical red lines border the region in which multiple mass flow rates are possible for a single heating power. This is the Ledinegg unstable region. Figure adopted from Krijger [1].

4.3.2. Frequency analysis

For each point found to be dynamically unstable, the imaginary part is also analysed. The imaginary part of the eigenvalue with the largest real part gives the resonance frequency of the system:

$$f_{res} = \Im\{\lambda\}$$

Krijger's code includes the display of maps containing this frequency information, shaded according to the frequency. However, since, in these figures, dynamically unstable points with zero frequency are indistinguishable from dynamically stable points, these frequency maps alone do not completely represent the dynamic stability of the system.

4.3.3. Parametric study

To investigate the influence a certain parameter has on the stability of the system, Krijger implemented code to display the neutral stability boundaries for various values of a parameter in a single figure. This allows for easy comparison of the stability of the system under different circumstances. The neutral stability boundaries are found in MATLAB by locating every element with value 1 that has at least one neighbouring 0.

5

Results

In this chapter, the results of the stability analysis outlined in the previous chapters are presented. Comparisons are made to the cases evaluated by Krijger and Lippens. First, a reference case is analysed. Then, a ceteris paribus parametric study is performed to identify the influence of the studied parameters on the stability of the loop. Finally, Ledinegg instabilities are analysed.

All results are presented in the form of stability maps or NSBs on a nondimensional plane. They include a diagonal black line marking the border between the use of the low heating and high heating models, which lies at $N_{sub} = N_{\Delta h}$. Because the approximations used in the model are not continuous around the pseudo-critical point, the boundary often marks a sharp transition from stable to unstable conditions.

5.1. Reference case

In his thesis, Krijger set up a reference case for his parametric study. The reference case was extended by Lippens for his inclusion of the wall thermal inertia effects. In this thesis, the reference case is further extended to also cover neutronics and fuel heat transfer. This extended case is referred to as the reference case in this chapter. The reference cases established and evaluated by Krijger and Lippens are referred to as the Krijger case and the Lippens case respectively. Many reference case parameters were adopted from the HPLWR model by Ortega Gómez [3]. The fuel heat transfer time constant reference value is $\tau = 6$s. The fuel enrichment is taken as $\varepsilon = 4\%$. The full list of parameters and their numerical values can be found in appendix C. The stability map for the reference case is shown in figure 5.1.

The reference case stability map shows obvious similarities to the case evaluated by Lippens: two unstable areas at the top center and top right of the map. In fact, the unstable area in the top-right corner remains entirely unaffected by the introduction of neutronics and fuel heat transfer. The inclusion of neutronics and heat transfer in the model appears to have a slight destabilising effect, as evidenced by the increased size of the unstable area in the top center and the appearance of an unstable area in the low heating regimen, to the top-left of the $N_{sub} = N_{\Delta h}$-line.
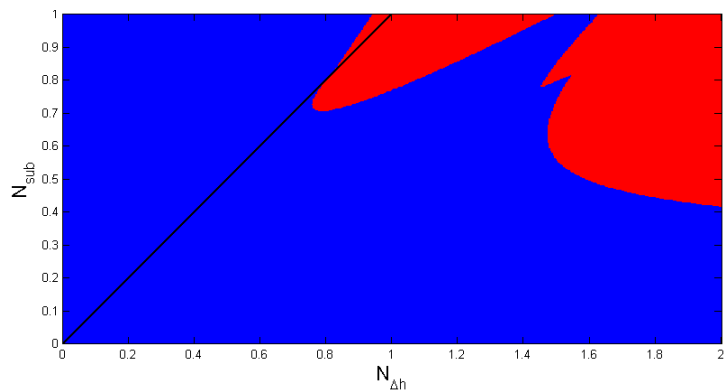
Figure 5.1: Stability map for the reference case.

When the density reactivity feedback coefficient α_r is turned down to zero, no neutronics effects take place. Therefore, one would expect the instability map to reflect the scenario analysed by Lippens.

As figure 5.2 shows, this is indeed the case. Adjusting the wall cross-sectional area to zero as well returns us to the Krijger case. This is shown in figure 5.3. These results show that the benchmark posed in section 4.1 is adhered to.
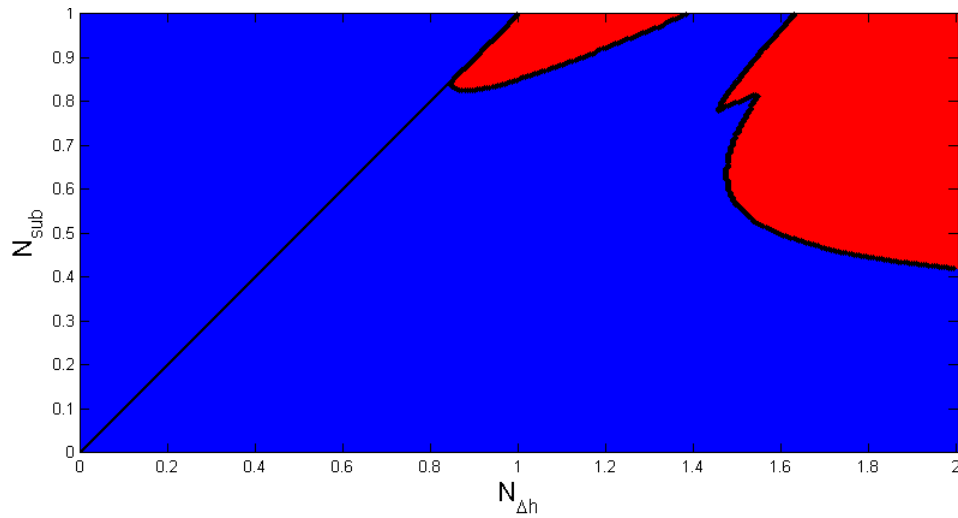
Figure 5.2: Stability map for the case with density reactivity feedback disabled. The neutral stability boundary for the Lippens case is overlaid in black.
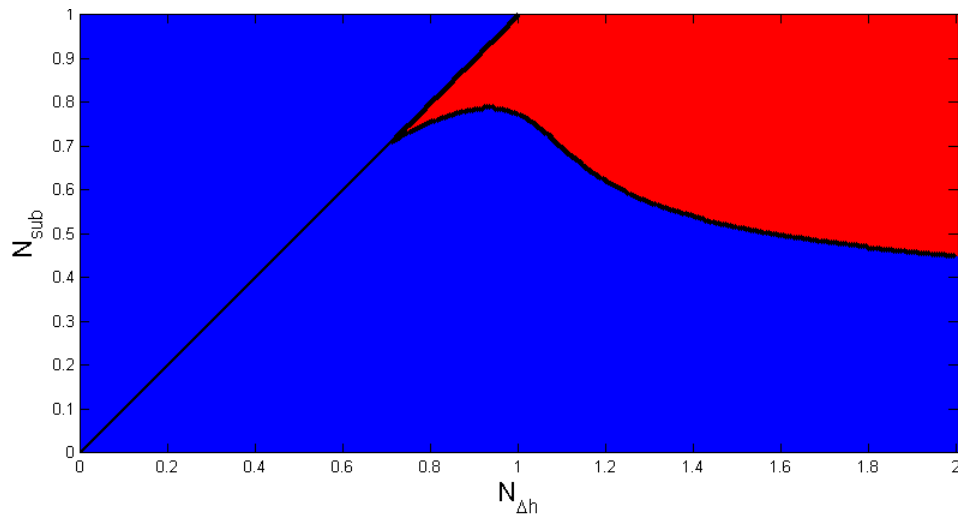
Figure 5.3: Stability map for the case with density reactivity feedback and wall thermal inertia disabled. The neutral stability boundary for the Krijger case is overlaid in black.

The effects of altering the density reactivity feedback are further investigated in the next section.

5.2. Parametric study

5.2.1. Fuel heat transfer time constant

The influence of the numerical value of the fuel heat transfer time constant is analysed through a ceteris paribus parametric study. Besides values between $\tau = 2$ s and $\tau = 6$ s, as proposed by Van der Hagen [18], more extreme values are studied as well. As figure 5.4 shows, increasing τ slightly increases instability. The unstable area reaches slightly lower values of N_{sub}. The rightmost unstable area is unaffected. While the destabilising effect of the fuel heat transfer model is no surprise, its influence was expected to be limited to the rightmost unstable area. Because the fuel dynamics affect

only the core, this should influence the higher-frequency Type-II instability domain. The area affected was previously considered the Type-I domain. This means that either this division is incorrect, and Type-II instabilities are present in the top-center area of the stability map as well, or the fuel dynamics somehow influence Type-I instabilities.
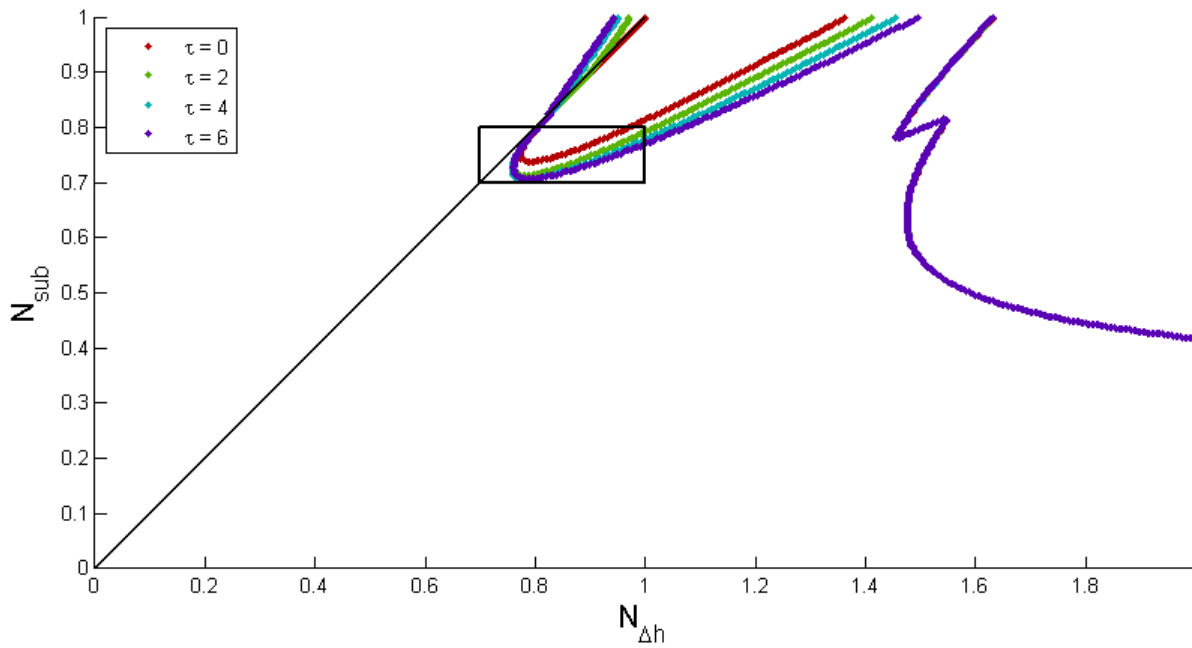
Figure 5.4: Neutral stability boundaries for heat transfer time constants in the range proposed by Van der Hagen. The boundary of the unstable area on the far right side remains the same independently of τ. The boxed area is magnified in figure 5.8.
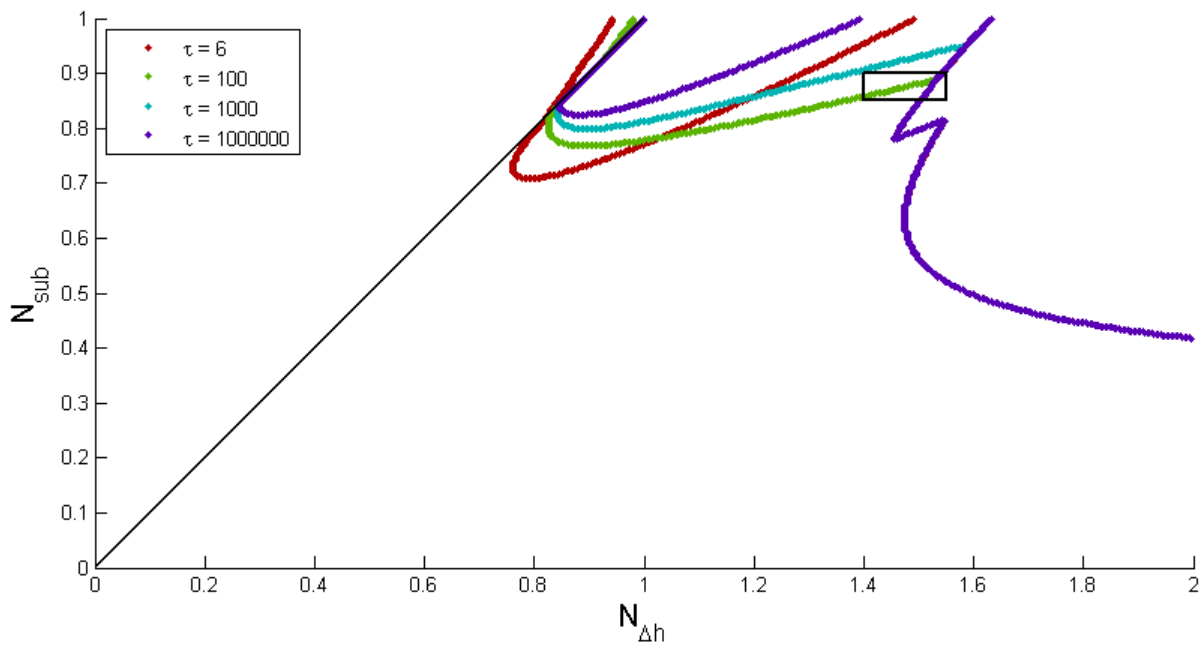
Figure 5.5: Neutral stability boundaries for heat transfer time constants well above the proposed range. The boxed area is magnified in figure 5.9.

In figure 5.5, higher values of τ are compared. Above $\tau = 6$ s, the water loop becomes stable for higher values of N_{sub} in the medium-$N_{\Delta h}$ region, but the upward trend of the NSB for increasing $N_{\Delta h}$

decreases. As τ is increased further, the dynamics of heat generation in the fuel take longer to affect the temperature of the coolant, and so the effect of the fuel rod heat transfer model diminishes. At large enough values of τ, the model returns to the case with no reactivity feedback at all – Lippens' case. Once again, the unstable area at the far right does not change depending on τ. To further analyse this behaviour, the resonance frequencies of the instabilities are studied.
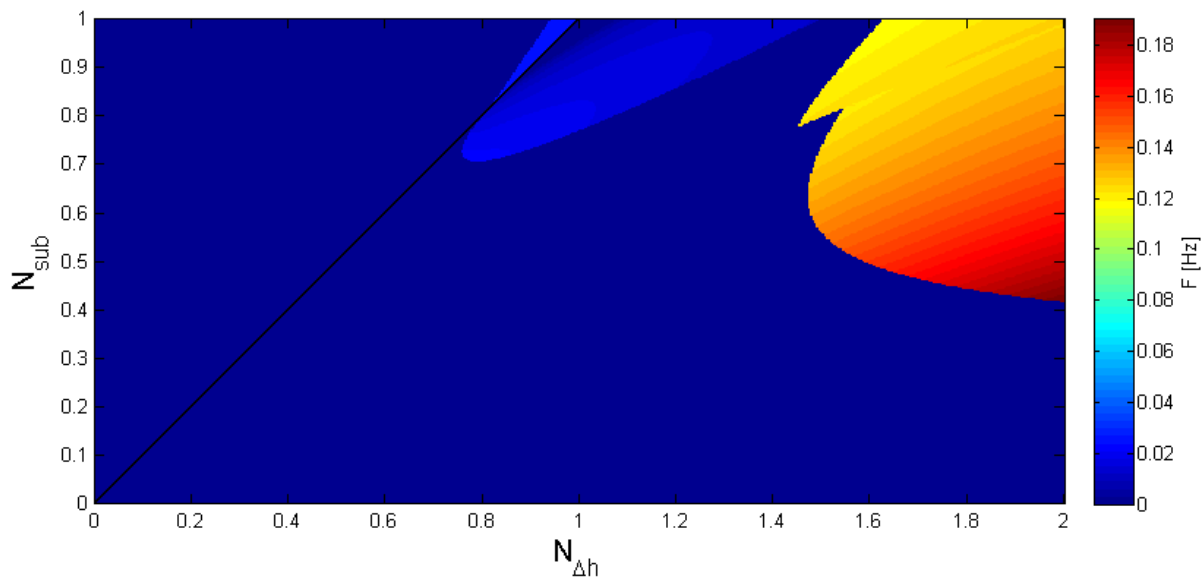
Figure 5.6: Resonance frequency map for the reference case.
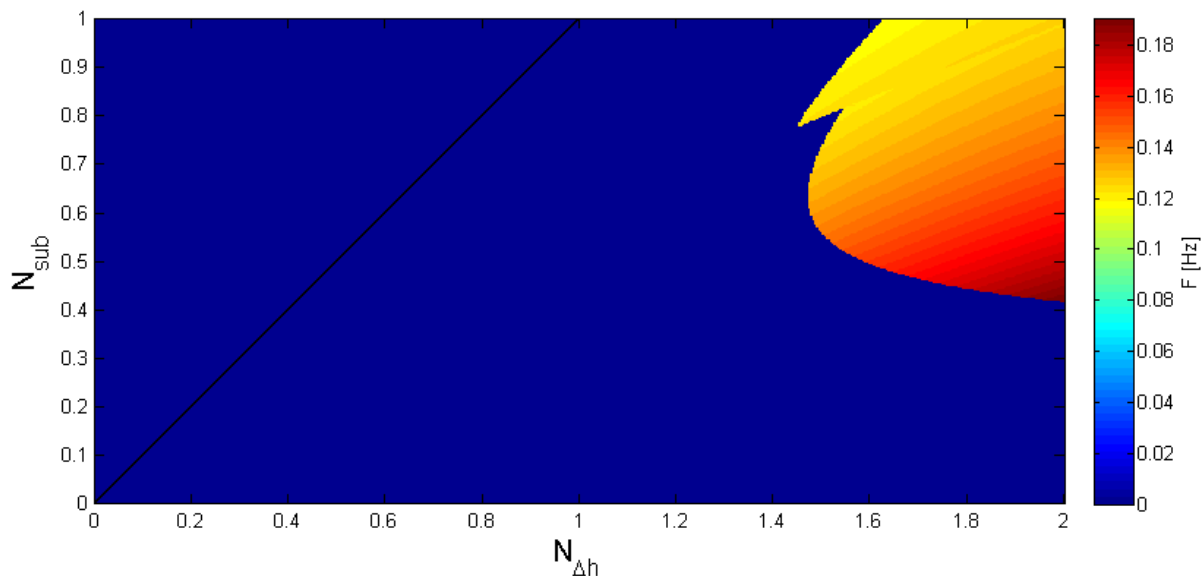
Figure 5.7: Resonance frequency map for $\tau = 10^9$ s.

Lippens found the unstable area at medium $N_{\Delta h}$ ($N_{\Delta h} \approx 1$) to have no dynamic instabilities, as frequency maps showed no resonance frequencies in that region for his case. He posited that the area was Ledinegg unstable. As figure 5.7 shows, in the case of extremely high τ, this is still apparent.

Figure 5.6 shows that low-frequency instabilities have arisen in most of the medium-$N_{\Delta h}$ region, while a small area close to $N_{sub} = 1, N_{\Delta h} = 1$ still exhibits instabilities with no frequency. The dynamic instabilities present have frequencies in the order of 0.01 Hz. This gives rise to the presumption that

this area is dominated by Type-I instabilities. As Krijger and Lippens both found, the area to the right is more likely to be Type-II unstable, as the instabilities in that region oscillate with higher frequencies. However, since the influence of τ is contained to the core, varying this parameter is expected to affect Type-II instabilities. As this appears not to be the case, there is perhaps still something to be learned about the nature of these instabilities in natural circulation HPLWRs.

Figures 5.4 and 5.5 show that there are two distinct points in the range of τ where the behaviour of the NSB as τ is increased changes. As τ is increased from zero, initially the NSB of the entire central unstable region comes down. After a certain point, around $\tau = 6$ s, the NSB no longer descends in the region around $N_{\Delta h} \approx 0.8$ as τ is increased, but keeps coming down farther at higher $N_{\Delta h}$. This continues until $\tau \approx 100$ s, after which the unstable area starts shrinking again, until finally reaching the case with no feedback present as τ approaches 10^6 s. To more accurately determine the values of τ at which these changes in behaviour occur, two more parametric studies are performed around the approximated cutoff values.

Figures 5.8 and 5.9 show magnified portions of figures 5.4 and 5.5 respectively. The stability boundary around $N_{\Delta h} \approx 0.8$ reaches the lowest point for $\tau \approx 4.5$ s. The lowest point near $N_{\Delta h} \approx 1.5$ is reached when $\tau \approx 100$ s. Because these values cannot be obtained algebraically, but only through trial and error, they are only approximations. Nevertheless, they give good indications of the time scales at which these changes in behaviour take place.
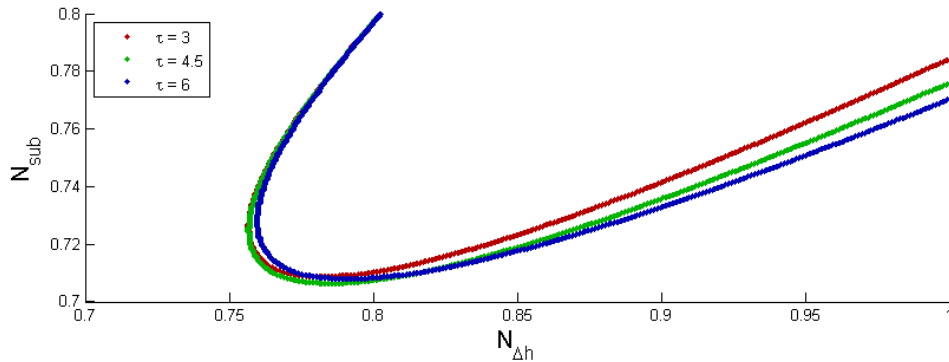
Figure 5.8: Detail of NSBs for τ around the first cutoff point. Past $\tau = 4.5$ s, the unstable area starts receding at its low-$N_{\Delta h}$ end.
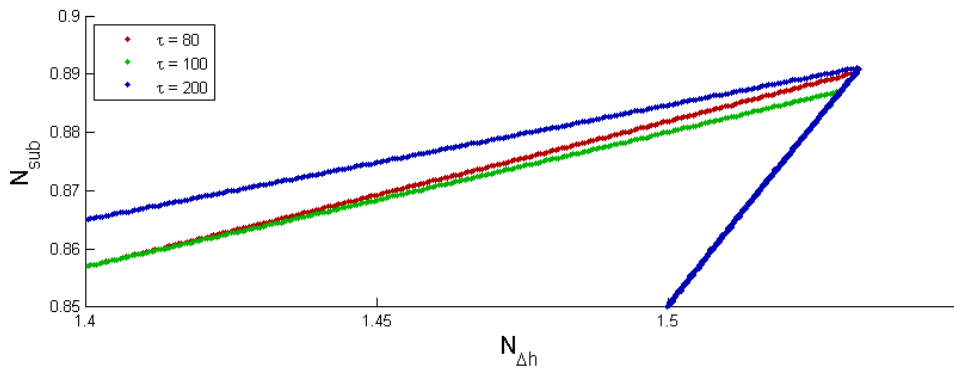
Figure 5.9: Detail of NSBs for τ around the second cutoff point. Past $\tau \approx 120$ s, the unstable area starts receding at the high-$N_{\Delta h}$ end.

Now that the effect of varying τ has been established, a final comparison can be made to confirm that the model with extremely high τ is in fact identical to the model with no feedback implemented. Figure 5.10 shows the NSB for a model with no feedback marked in red crosses. The reference case, where $\tau = 6$ s and $\alpha_r = \alpha_{r,ref}$, is included as a baseline. The blue line indicates the NSB for extremely high τ, with normal density reactivity feedback as in the reference case. The boundaries marked in red and blue coincide, showing that the models are identical. That this should be the case can be easily seen by looking at equation 2.41. For large enough τ, the time-derivative of $\check{q}_w$ vanishes, so that equation 2.40 reduces to the form derived by Lippens [2], with no reactivity feedback.
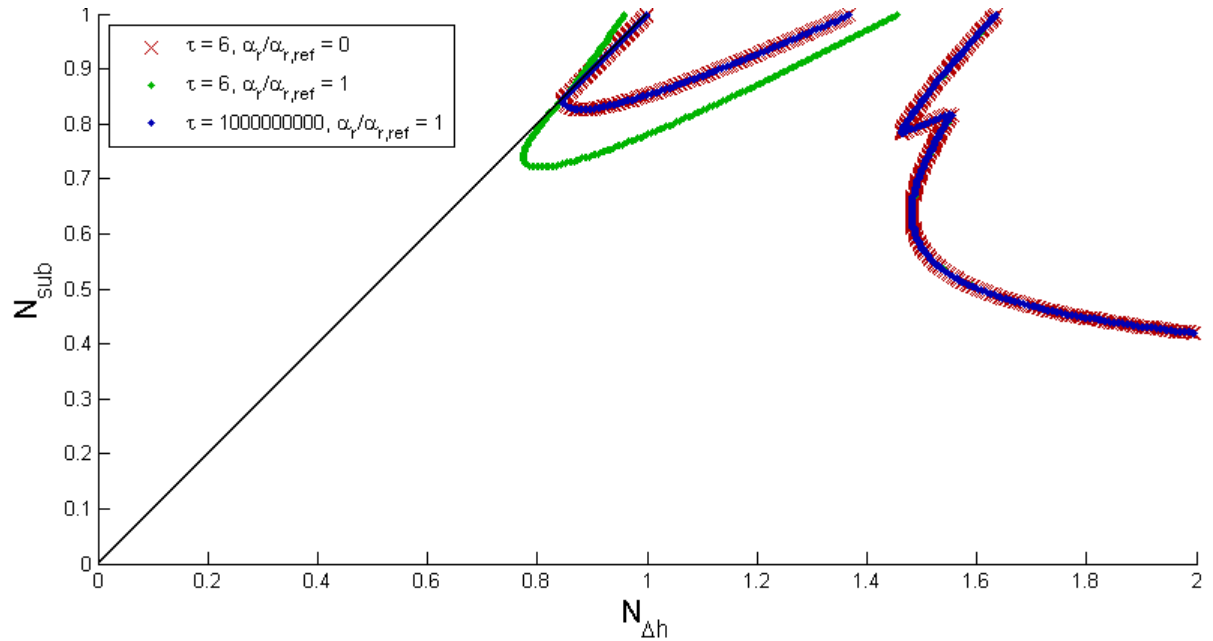
Figure 5.10: Neutral stability boundaries for the reference case and two separate ways of modelling a case without feedback; reducing α_r to zero and increasing τ to very large values.

5.2.2. Density reactivity feedback coefficient

A single parametric study on the behaviour of the system under changes of the density reactivity feedback coefficient is conducted. Figure 5.11 shows the NSB for the cases with no feedback, the reference case, and two cases with doubled and tripled feedback. Once again, the instability domain in the high-$N_{\Delta h}$ region is unaffected by the changes. The unstable areas at medium $N_{\Delta h}$ in both the low and high heating sections of the stability map grow with increasing α_r. This effect is far more evident than that of varying τ.

The sharp transition on the $N_{sub} = N_{\Delta h}$-line is likely caused by the discontinuity of the approximations used in the model. For $\alpha_r = \alpha_{r,ref}$, the transition appears quite smooth, but higher values of α_r break that illusion and show a sudden jump in the NSB.

The frequency map of the case with tripled feedback, in figure 5.12, shows that the frequency of oscillation in these areas, while higher than in the reference case, is still much lower than that of the far-right unstable area. The instabilities in the low heating section oscillate at frequencies of approximately 0.035 Hz, while the frequencies in the high heating, medium-$N_{\Delta h}$-region vary between 10^{-4} and 0.03 Hz, indicating that they are likely to be of the same type.

The unstable area in the far right is unaffected by both variations in τ and α_r, and Lippens was also unable to influence that area through thermodynamic effects. Krijger's parametric studies on the geometry of the channel, however, did show noticeable influence on that area. This leads to the possibility that the instabilities in that area are caused by flow geometry concerns, whereas the influence of neutronics and thermodynamics is more likely confined to the affected area near $N_{\Delta h} = 1$.
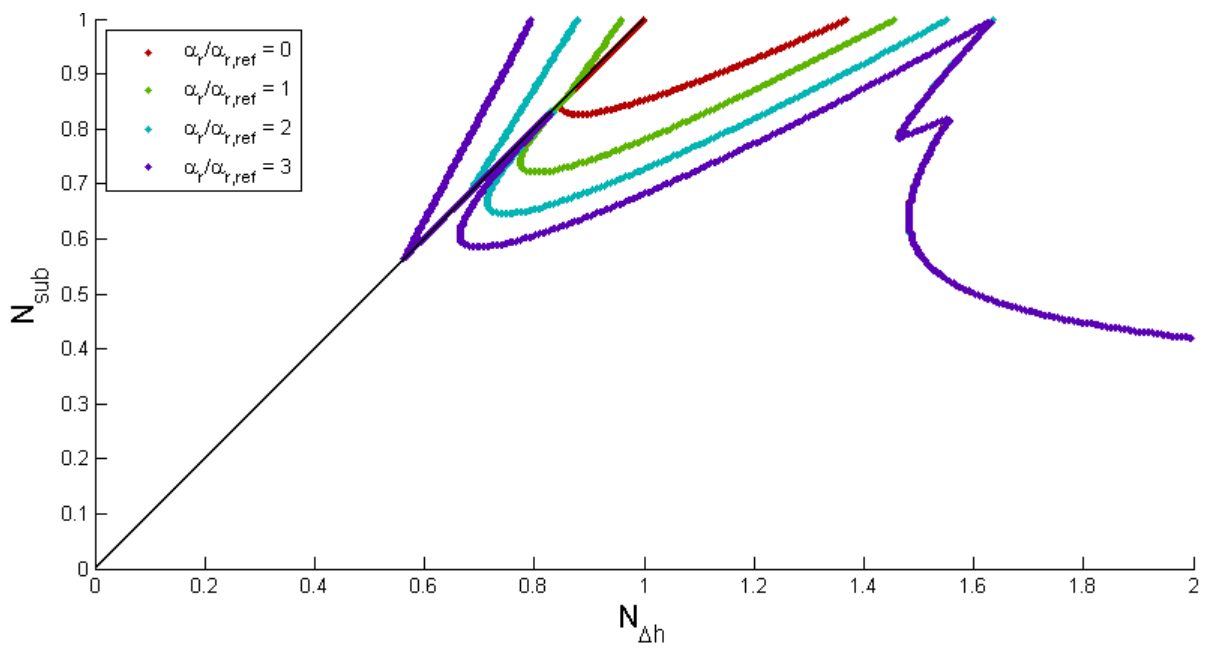
Figure 5.11: Neutral stability boundaries for the parametric study on the density reactivity feedback coefficient, α_r.
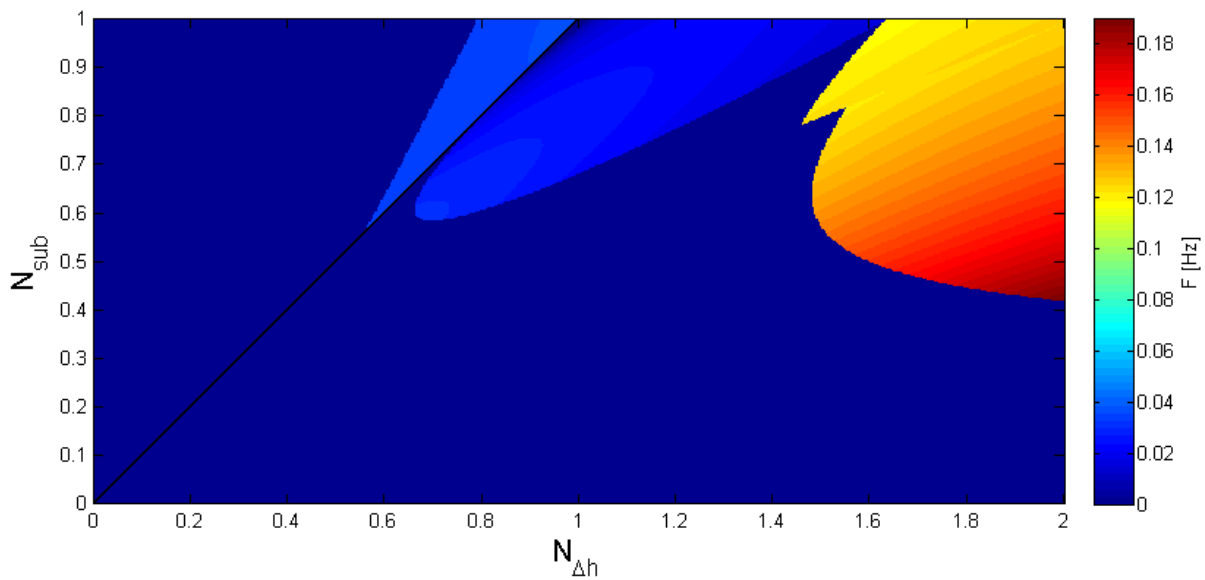
Figure 5.12: Resonance frequency map for $\alpha_r = 3\alpha_{r,ref}$.

5.2.3. Fuel enrichment

Since the fuel enrichment, ε, is present in the balance equations governing the system (see equations 2.11 through 2.16), variations thereof should affect the stability of the system. As figure 5.13 shows, however, this does not seem to be the case.
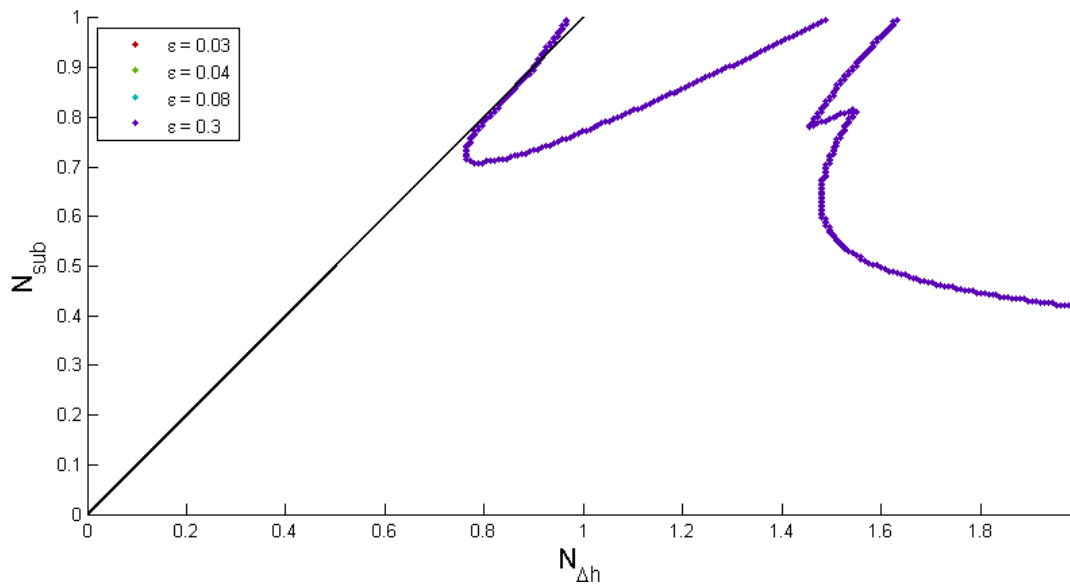
Figure 5.13: Neutral stability boundaries for various fuel enrichments ε. All boundaries coincide — the enrichment appears to have no effect on the stability.

It is unclear why the stability of the model seems unaffected by the fuel enrichment. Possible explanations are that the enrichment does affect certain instabilities, but these are drowned out by much larger instabilities also present, or that the nature of the model — looking at perturbations only, and subtracting the steady state values from the balances — causes the enrichment to have no effect.

5.3. Ledinegg instabilities

Using Krijger's code to search for Ledinegg instabilities results in a single Ledinegg unstable region in the same location as found by Krijger and Lippens. This Ledinegg unstable area partially coincides with dynamically unstable points. The presence of dynamic instabilities therefore does not preclude the presence of static instabilities.

Figure 5.14 shows the Ledinegg map for the reference case superimposed on the stability map. The newly arisen unstable area in the low heating section of the map does not appear Ledinegg unstable. The Ledinegg unstable area shows obvious similarities to the cases investigated by Lippens and Krijger. A comparison of the Ledinegg stability boundaries, shown in figure 5.15, shows that the Ledinegg unstable area is indeed unchanged from Krijger's work. Lippens also found the Ledinegg unstable area to match up with Krijger's.

It is not surprising that the neutronics and fuel heat transfer do not affect the Ledinegg instability of the system. Since Ledinegg instabilities are static, not dynamic instabilities, their cause must be found in the steady-state system. In the linearised model used in this research, the neutronics and fuel heat transfer do not affect the steady state, and therefore should — and do — not affect the Ledinegg instability.
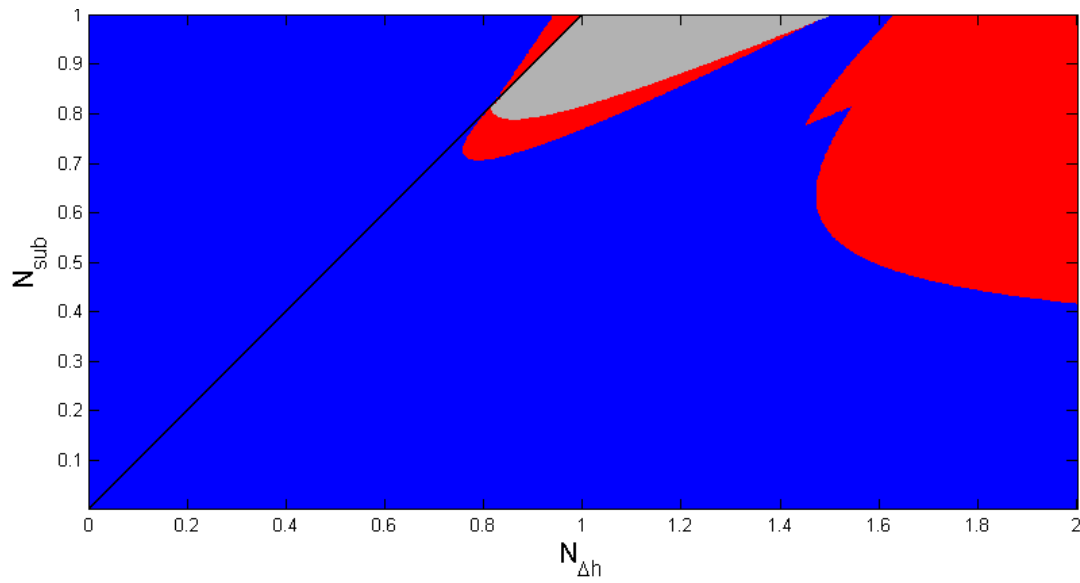
Figure 5.14: Ledinegg map for the reference case. The gray region marks the possibility of Ledinegg instabilities.
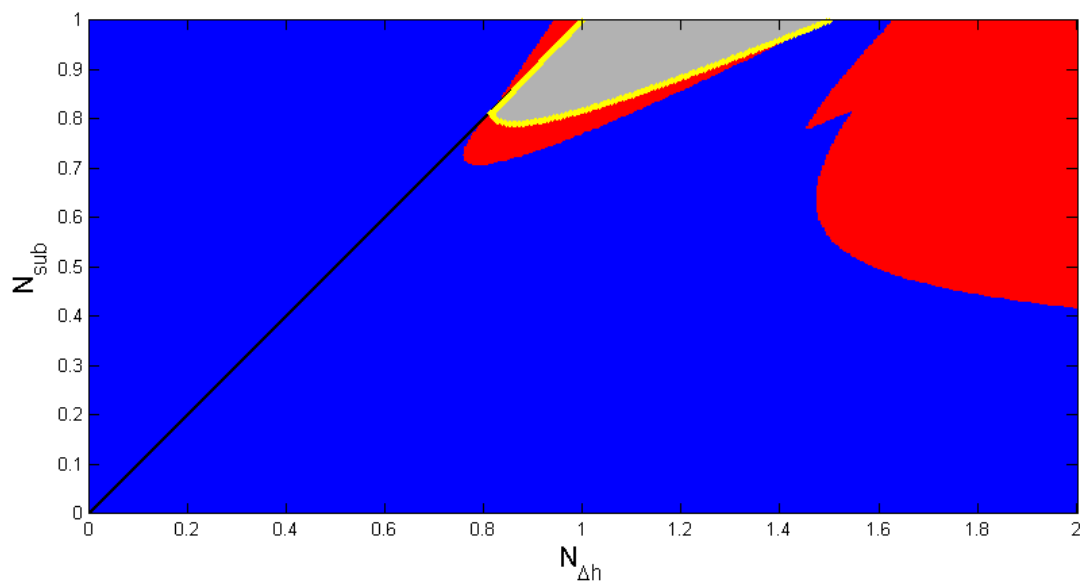
Figure 5.15: Ledinegg map for the reference case, with the Ledinegg stability boundary from Krijger's case overlaid in yellow. The Ledinegg unstable regions coincide entirely.

6

Conclusions and Discussion

6.1. Conclusions

The model developed by Krijger and augmented by Lippens has been successfully extended to also include neutronics and fuel heat transfer. The reference case has also been extended to include these effects. Instability characteristics have been calculated for the reference case, and parametric studies have been performed on the heat transfer time constant, the density reactivity feedback coefficient, and the enrichment. From the results, we can draw the following conclusions.

Introducing neutronics and fuel heat transfer to the system has a destabilising effect. Increasing the fuel heat transfer time constant beyond $\tau \approx 4.5$ s, up to $\tau \approx 100$ s, improves stability at $N_{\Delta h} \approx 0.8$, while making the system less stable at $N_{\Delta h} \approx 1.5$. Further increasing τ diminishes the destabilising effect, until finally the effect of the neutronics disappears as τ approaches 10^6 s. This is expected, and can be concluded from examining equations 2.41 and 2.40. τ is suspected to lie between 2 and 6 s, around the peak of the destabilising effect near $N_{\Delta h} = 0.8$.

The introduction of density reactivity feedback has a stronger destabilising effect than the fuel heat transfer for the values investigated in this research. The feedback also gives rise to a new unstable region in the low heating zone. No unstable areas were found in the low heating model in the reference cases studied by Krijger and Lippens, but the extended model studied in this thesis shows that the low heating model is not uniformly stable at reference case conditions. Increasing the magnitude of the density reactivity feedback coefficient has a destabilising effect on the area near $N_{\Delta h} = 1$, in agreement with findings by Van Bragt for BWRs [10].

The Ledinegg unstable area remains unchanged from the case with no neutronics and fuel heat transfer implemented. The newly arisen unstable area in the low heating region contains no Ledinegg instabilities. It can be concluded that the neutronic-thermal-hydraulic coupling does not affect the steady state. This is not surprising, since density reactivity feedback relies on changes in density, of which there are none in a steady-state scenario. While Krijger and Lippens only found Ledinegg instabilities where the resonance frequency maps showed no resonance, Ledinegg instabilities have now arisen in unstable areas with nonzero resonance frequencies as well. Krijger already asserted that his method for finding Ledinegg instabilities could not give a decisive answer about Ledinegg unstable areas, and further improvements to the method do seem necessary.

The fuel enrichment appears not to affect the stability of the system.

6.2. Discussion and recommendations

The fact that the stability of the system does not seem to be affected by altering the fuel enrichment parameter in the code calls for further investigation. If the independence on enrichment is caused by the enrichment-based instabilities being drowned out by larger instabilities, it may not be possible to further investigate the cause. The code could be altered to show which of the eigenvalues are resulting in instabilities, but this might not provide conclusive evidence. Nevertheless, it may be worth looking into. Knowing which eigenvalues are responsible for the destabilisation of the system may be invaluable for a thorough understanding of the mechanics.

Additionally, the accuracy of the fuel rod heat transfer model may be greatly improved. In this thesis, the fuel was treated as a single node. This means density reactivity feedback is considered uniform throughout the fuel. In practice, the axial position of the fuel is very significant in determining the feedback. The diffusion length of neutrons is in the order of only a few centimeters, and as such, considering the core is several meters in length, feedback in the top and bottom of the core are entirely different. While dividing the fuel up into two nodes, as is done with the core and wall for the low and high heating models, will slightly improve the accuracy of the feedback calculations, the model will remain far from the real case. Dividing the fuel and the core up into several shorter nodes, so that density reactivity feedback and fuel heat transfer may be calculated separately in each of them, will greatly increase the complexity of the model and detract from its computational speed.

A point of attention is the previously hypothesised divide between Type-I and Type-II unstable areas in the stability maps. While the top-centre unstable area was thought to be Type-I-unstable, and the far right unstable area Type-II, the introduction of neutronics has only affected the top-centre area. Since neutronics, being a core effect, should influence only Type-II instabilities, these areas may have been attributed the wrong kind of instability. Further investigation into the nature of the instabilities in the two distinguishable areas is therefore advised.

Finally, the conclusions reached in this research are not discouraging for the development of the natural circulation driven HPLWR. While the introduction of neutronics has increased instability of the system, this was expected based on prior research on other natural circulation driven reactor types. All in all, the natural circulation driven HPLWR seems a promising reactor design.

A

Coefficient Matrices

This appendix presents the coefficient matrices A and B that have been used in the stability analyses in this work. Because of the large size of the matrices, they have been split up into parts.

A.1. Low heating model

Coefficient matrix A:

Columns 1 to 5

$$
\begin{pmatrix}
\frac{1}{2}C_1 N_{\Delta h} h_{pc} v_{pc} & C_1 N_{\Delta h} h_{pc} v_{pc} \underline{L_R} & 0 & 0 & 0 \\
\frac{1}{2}(C_1 N_{\Delta h} h_{pc} v_{pc} \overline{H}_0 + \underline{\rho_0} & C_1 N_{\Delta h} h_{pc} v_{pc} \overline{H}_{out} \underline{L_R} & 0 & 0 & 0 \\
0 & \underline{L_R \overline{\rho}_R} + \underline{L_R} C_1 N_{\Delta h} h_{pc} v_{pc} (\underline{\overline{H}_R} - \underline{\overline{H}_{out}}) & 0 & 0 & 0 \\
0 & 0 & 1 + \underline{L_D} + \overline{V}_B & \underline{L_R} & 0 \\
0 & 0 & 0 & 0 & \underline{\rho_w c_{p,w} A_w} \\
0 & \cdots & & & 0 \\
\vdots & \ddots & & & \vdots \\
0 & \cdots & & & 0
\end{pmatrix}
$$

Colums 6 to 13

$$
\begin{pmatrix}
0 & & \cdots & & & & & 0 \\
0 & & & & & & & \\
0 & & & \ddots & & & & \vdots \\
0 & & & & & & & \\
0 & & & \cdots & & & & 0 \\
1 & 0 & 0 & 0 & 0 & 0 & 0 & 0 \\
0 & 1 & 0 & 0 & 0 & 0 & 0 & 0 \\
0 & 0 & 1 & 0 & 0 & 0 & 0 & 0 \\
0 & 0 & 0 & 1 & 0 & 0 & 0 & 0 \\
0 & 0 & 0 & 0 & 1 & 0 & 0 & 0 \\
0 & 0 & 0 & 0 & 0 & 1 & 0 & 0 \\
0 & 0 & 0 & 0 & 0 & 0 & 1 & 0 \\
0 & 0 & 0 & 0 & 0 & 0 & 0 & \underline{\tau}
\end{pmatrix}
$$

Coefficient matrix B:
Column 1

$$
\begin{pmatrix}
0 \\
-\left(\widehat{Nu_0}\frac{P_{in}}{\overline{\underline{D_H}}}\left(\left(\underline{\alpha_0}\left(\underline{H_0}-\underline{h_{pc}}\right)+\frac{1}{2\underline{c_{p,pc}}}\right)\overline{\lambda}_{f0}^{0.34}-0.17\overline{\lambda}_{f0}^{-0.66}\left(\overline{T}_w-\overline{T}_0\right)\underline{\beta_0}\right)+1\right) \\
1 \\
\frac{1}{2}C_1 N_{\Delta h}h_{pc}v_{pc}\left(\frac{1}{2}\left(\frac{f_0}{\overline{\underline{D_H}}}+K_0\right)\frac{1}{\overline{\underline{\rho}}_0^{2}}-\frac{1}{N_{Fr}}\right) \\
\frac{1}{2}\widehat{Nu_0}\frac{P_{in}}{\overline{\underline{D_H}}}\left(\overline{\lambda}_{f0}^{0.34}\left(2\underline{\alpha_0}\left(\underline{H_0}-\underline{h_{pc}}\right)+\frac{1}{\underline{c_{p,pc}}}\right)-0.34\overline{\lambda}_{f0}^{-0.66}\left(\overline{T}_w-\overline{T}_0\right)\underline{\beta_0}\right) \\
\frac{C_1 N_{\Delta h}h_{pc}v_{pc}\underline{\alpha_r}\overline{n}}{2\underline{\Lambda}} \\
0 \\
0 \\
0 \\
0 \\
0 \\
0 \\
0
\end{pmatrix}
$$

Columns 2, 3

$$
\begin{pmatrix}
0 & 1 \\
0 & \frac{1}{\overline{H}_{in}} \\
-1 & 0 \\
\frac{1}{2}C_1 N_{\Delta h}h_{pc}v_{pc}\left(\frac{1}{2}\left(\frac{f_R L_R}{\overline{\underline{D_H}}}+K_R\right)\frac{1}{\overline{\underline{\rho}}_R^{2}}-\frac{L_R}{N_{Fr}}\right) & \left(\underline{v_{in}}\left(\frac{f_0}{\overline{\underline{D_H}}}+K_0\right)\overline{v}_0-\left(\frac{f_D L_D}{\overline{\underline{D_H}}}+K_D\right)\underline{v_{in}}\right) \\
0 & 0 \\
0 & 0 \\
0 & 0 \\
0 & 0 \\
0 & 0 \\
0 & 0 \\
0 & 0 \\
0 & 0 \\
0 & 0
\end{pmatrix}
$$

Columns 4, 5, 6

$$
\begin{pmatrix}
-1 & 0 & 0 \\
-\overline{H}_{out} & \widehat{Nu_0}\overline{\lambda}_{f0}^{-0.34}\frac{P_{in}}{\overline{\underline{D_H}}} & 0 \\
\overline{H}_{out}-\overline{H}_R & 0 & 0 \\
-\left(\left(\frac{f_R L_R}{\overline{\underline{D_H}}}+K_R\right)\overline{\underline{v}}_R+\underline{v_{in}}\right) & 0 & 0 \\
0 & -\widehat{Nu_0}\overline{\lambda}_{f0}^{-0.34}\frac{P_{in}}{\overline{\underline{D_H}}} & 0 \\
0 & 0 & -\frac{\beta}{\underline{\Lambda}} \\
0 & 0 & \frac{\beta_1}{\underline{\Lambda}} \\
0 & 0 & \frac{\beta_2}{\underline{\Lambda}} \\
0 & 0 & \frac{\beta_3}{\underline{\Lambda}} \\
0 & 0 & \frac{\beta_4}{\underline{\Lambda}} \\
0 & 0 & \frac{\beta_5}{\underline{\Lambda}} \\
0 & 0 & \frac{\beta_6}{\underline{\Lambda}} \\
0 & 0 & \Sigma_f E_f \overline{V_f}v_n
\end{pmatrix}
$$

Columns 7 to 13

$$
\begin{pmatrix}
0 & & & \cdots & & & 0 \\
0 & & & & & & \\
0 & & & \ddots & & & \vdots \\
0 & & & & & & 0 \\
0 & & & \cdots & & 0 & 1 \\
\lambda_1 & \lambda_2 & \lambda_3 & \lambda_4 & \lambda_5 & \lambda_6 & 0 \\
-\underline{\lambda_1} & 0 & 0 & 0 & 0 & 0 & 0 \\
\underline{0} & -\underline{\lambda_2} & 0 & 0 & 0 & 0 & 0 \\
0 & \underline{0} & -\underline{\lambda_3} & 0 & 0 & 0 & 0 \\
0 & 0 & \underline{0} & -\underline{\lambda_4} & 0 & 0 & 0 \\
0 & 0 & 0 & \underline{0} & -\underline{\lambda_5} & 0 & 0 \\
0 & 0 & 0 & 0 & \underline{0} & -\underline{\lambda_6} & 0 \\
0 & 0 & 0 & 0 & 0 & \underline{0} & -1
\end{pmatrix}
$$

A.2. High heating model

Coefficient matrix A:
Columns 1 to 3

$$
\begin{pmatrix}
\underline{\rho_0 \left(\frac{H_0}{\underline{h_{pc}}} - 1 \right)} & 0 & 0 \\[2ex]
\left(\frac{1}{\underline{v_1}} - \frac{H_0}{\underline{h_{pc}}} \underline{\rho_0} \right) & -\dfrac{\underline{\overline{L}_1} C_1 N_{\Delta h} h_{pc}}{vpc \overline{v}_1^2} & 0 \\[3ex]
0 & 0 & -\dfrac{\underline{\overline{L}_R} C_1 N_{\Delta h} h_{pc}}{vpc \overline{v}_R^2} \\[3ex]
\left(\underline{\frac{\overline{H}_1}{\overline{v}_1}} - \underline{H_0 \rho_0} \right) & \underline{\frac{\overline{L}_1}{\overline{v}_1}} \left(1 - \dfrac{\overline{H}_1 C_1 N_{\Delta h} h_{pc}}{vpc \overline{v}_1} \right) & 0 \\[3ex]
0 & 0 & \left(\underline{L_R \overline{\rho}_R} - \underline{L_R} C_1 N_{\Delta h} h_{pc} v_{pc} (\overline{H}_R - \overline{H}_{out}) \right) \\[2ex]
0 & 0 & 0 \\
-\underline{\rho_w c_{p,w} A_w \overline{T}_{w,0}} & 0 & 0 \\
\underline{\rho_w c_{p,w} A_w \overline{T}_{w,1}} & 0 & 0 \\
0 & 0 & 0 \\
\vdots & \vdots & \vdots \\
0 & 0 & 0
\end{pmatrix}
$$

Columns 4 to 8

$$
\begin{pmatrix}
0 & & \cdots & & 0 \\
0 & & & & \\
0 & & \ddots & & \vdots \\
0 & & & & \\
0 & & \cdots & & 0 \\
1 - \underline{\overline{L}_1} + \underline{L_D} + \overline{V}_B & \underline{\overline{L}_1} & \underline{L_R} & 0 & 0 \\
0 & 0 & 0 & \underline{\rho_w c_{p,w} A_w \overline{L}_0} & 0 \\
0 & 0 & 0 & 0 & \underline{\rho_w c_{p,w} A_w \overline{L}_1} \\
0 & 0 & 0 & 0 & 0 \\
\vdots & & \vdots & & \vdots \\
0 & & 0 \;\; 0 & 0 & 0
\end{pmatrix}
$$

Colums 9 to 16

$$
\begin{pmatrix}
0 & & \cdots & & & & & 0 \\
0 & & & & & & & \\
0 & & & & & & & \\
0 & & \ddots & & & & & \vdots \\
0 & & & & & & & \\
0 & & & & & & & \\
0 & & & & & & & \\
0 & & \cdots & & & & & 0 \\
1 & 0 & 0 & 0 & 0 & 0 & 0 & 0 \\
0 & 1 & 0 & 0 & 0 & 0 & 0 & 0 \\
0 & 0 & 1 & 0 & 0 & 0 & 0 & 0 \\
0 & 0 & 0 & 1 & 0 & 0 & 0 & 0 \\
0 & 0 & 0 & 0 & 1 & 0 & 0 & 0 \\
0 & 0 & 0 & 0 & 0 & 1 & 0 & 0 \\
0 & 0 & 0 & 0 & 0 & 0 & 1 & 0 \\
0 & 0 & 0 & 0 & 0 & 0 & 0 & \underline{\tau}
\end{pmatrix}
$$

Coefficient matrix B:
Column 1

$$
\begin{pmatrix}
\frac{1}{h_{pc}} \\[4pt]
-\frac{1}{h_{pc}} \\[4pt]
0 \\[4pt]
\frac{P_{in}}{\underline{D_H}}\left(\widehat{\underline{Nu}_1}\,\overline{\underline{\lambda}}_{f1}^{-0.34}\left(\overline{T}_{w,1}-\overline{\underline{T}_1}\right)-\widehat{\underline{Nu}_0}\,\overline{\underline{\lambda}}_{f0}^{-0.34}\left(\overline{T}_{w,0}-\overline{\underline{T}_0}\right)\right) \\[4pt]
0 \\[4pt]
\frac{1}{2}\left(\frac{f_0 v_0}{\underline{D_H}}-\frac{f_1\overline{\underline{v}}_1}{\underline{D_H}}\right)+\frac{1}{N_{Fr}\underline{v}_0}-\frac{1}{N_{Fr}\overline{\underline{v}}_1} \\[4pt]
\widehat{\underline{Nu}_0}\,\overline{\underline{\lambda}}_{f0}^{-0.34}\frac{P_{in}}{\underline{D_H}}\left(\overline{T}_{w,0}-\underline{T}_0\right)-1 \\[4pt]
1-\widehat{\underline{Nu}_1}\,\overline{\underline{\lambda}}_{f1}^{-0.34}\frac{P_{in}}{\underline{D_H}}\left(\overline{T}_{w,1}-\overline{\underline{T}_1}\right) \\[4pt]
0 \\[4pt]
\vdots \\[4pt]
0
\end{pmatrix}
$$

Column 2

$$
\begin{pmatrix}
0 \\[4pt]
0 \\[4pt]
0 \\[4pt]
-\left(\widehat{\underline{Nu}_1}\frac{P_{in}\overline{L}_1}{\underline{D_H}}\left(\left(2\underline{\alpha}_1\left(\overline{H}_1-h_{pc}\right)+\frac{1}{c_{p,pc}}\right)\overline{\underline{\lambda}}_{f1}^{-0.34}+0.34\left(\overline{T}_{w,1}-\overline{\underline{T}_1}\right)\overline{\underline{\lambda}}_{f1}^{-0.66}\beta_1\lambda_z e^{-\beta_1\overline{H}_1}\right)+1\right) \\[4pt]
1 \\[4pt]
\left(-\frac{1}{2}\left(\frac{f_1\overline{L}_1}{\underline{D_H}}+K_1\right)+\frac{\overline{L}_1}{N_{Fr}\overline{\underline{v}}_R^2}\right)\frac{c_1 N_{\Delta h} h_{pc}}{vpc} \\[4pt]
0 \\[4pt]
\widehat{\underline{Nu}_1}\frac{P_{in}\overline{L}_1}{\underline{D_H}}\left(\left(2\underline{\alpha}_1\left(\overline{H}_1-h_{pc}\right)+\frac{1}{c_{p,pc}}\right)\overline{\underline{\lambda}}_{f1}^{-0.34}+0.34\left(\overline{T}_{w,1}-\overline{\underline{T}_1}\right)\overline{\underline{\lambda}}_{f1}^{-0.66}\beta_1\lambda_z e^{-\beta_1\overline{H}_1}\right) \\[4pt]
-\frac{c_2 N_{\Delta h} h_{pc}\alpha_r\overline{L}_1\overline{n}}{vpc\,\Lambda\overline{\underline{v}}_1^2} \\[4pt]
0 \\[4pt]
\vdots \\[4pt]
0
\end{pmatrix}
$$

Column 3

$$
\begin{pmatrix}
0 \\
0 \\
0 \\
0 \\
-1 \\
\left(-\dfrac{1}{2}\left(\dfrac{f_R \overline{L}_R}{\underline{D_H}} + K_R \right) + \dfrac{\overline{L}_R}{N_{Fr}\overline{v}_R^2} \right) \dfrac{C_1 N_{\Delta h} h_{pc}}{\upsilon pc} \\
0 \\
\vdots \\
0
\end{pmatrix}
$$

Columns 4, 5

$$
\begin{pmatrix}
1 - \dfrac{H_{in}}{\overline{\overline{h}}_{pc}} & 0 \\
\dfrac{H_{in}}{\overline{\overline{h}}_{pc}} & -1 \\
0 & 1 \\
H_{in} & -\overline{H}_1 \\
0 & \overline{H}_1 \\
-\left(\left(\dfrac{f_0 \overline{L}_0}{\underline{D_H}} + K_0 \right)\overline{v}_0 \left(\dfrac{f_D \overline{L}_D}{\underline{D_H}} + K_D \right)\overline{v_{in}} - \underline{v_{in}} \right) & -\left(\dfrac{f_1 \overline{L}_1}{\underline{D_H}} + K_1 \right)\overline{v}_1 \\
0 & 0 \\
\vdots & \vdots \\
0 & 0
\end{pmatrix}
$$

Columns 6, 7, 8

$$
\begin{pmatrix}
0 & 0 & 0 \\
0 & 0 & 0 \\
-1 & 0 & 0 \\
0 & \dfrac{\widehat{Nu_0}\,\overline{\lambda}_{f0}^{-0.34}\dfrac{P_{in}\overline{L}_0}{\underline{D_H}}}{} & \dfrac{\widehat{Nu_1}\,\overline{\lambda}_{f1}^{-0.34}\dfrac{P_{in}\overline{L}_1}{\underline{D_H}}}{} \\
-\overline{H}_R & 0 & 0 \\
-\left(\dfrac{f_R \overline{L}_R}{\underline{D_H}} + K_R + \dfrac{v_{in}}{\overline{\overline{v}}_R} \right)\overline{v}_R & 0 & 0 \\
0 & -\left(\widehat{Nu_0}\,\overline{\lambda}_{f0}^{-0.34}\dfrac{P_{in}\overline{L}_0}{\underline{D_H}} + 2\underline{\lambda}_w A_w \right) & 2\underline{\lambda}_w A_w \\
0 & 2\underline{\lambda}_w A_w & -\left(\widehat{Nu_1}\,\overline{\lambda}_{f1}^{-0.34}\dfrac{P_{in}\overline{L}_1}{\underline{D_H}} + 2\underline{\lambda}_w A_w \right) \\
0 & 0 & 0 \\
\vdots & \vdots & \vdots \\
0 & 0 & 0
\end{pmatrix}
$$

Columns 9 to 16

$$
\begin{pmatrix}
0 & & \cdots & & & & & 0 \\
0 & & & & & & & \\
0 & & \ddots & & & & & \vdots \\
0 & & & & & & & \\
0 & & & & & & & \\
0 & & & & & & & 0 \\
0 & & \cdots & & & & 0 & 1-L_1 \\
0 & & \cdots & & & & 0 & L_1 \\
-\dfrac{\beta}{\Lambda} & \lambda_1 & \lambda_2 & \lambda_3 & \lambda_4 & \lambda_5 & \lambda_6 & 0 \\
\dfrac{\bar{\beta}_1}{\Lambda} & -\lambda_1 & 0 & 0 & 0 & 0 & 0 & 0 \\
\dfrac{\bar{\beta}_2}{\Lambda} & 0 & -\lambda_2 & 0 & 0 & 0 & 0 & 0 \\
\dfrac{\bar{\beta}_3}{\Lambda} & 0 & 0 & -\lambda_3 & 0 & 0 & 0 & 0 \\
\dfrac{\bar{\beta}_4}{\Lambda} & 0 & 0 & 0 & -\lambda_4 & 0 & 0 & 0 \\
\dfrac{\bar{\beta}_5}{\Lambda} & 0 & 0 & 0 & 0 & -\lambda_5 & 0 & 0 \\
\dfrac{\bar{\beta}_6}{\Lambda} & 0 & 0 & 0 & 0 & 0 & -\lambda_6 & 0 \\
\Sigma_f E_f V_f v_n & 0 & 0 & 0 & 0 & 0 & 0 & -1
\end{pmatrix}
$$

B

Balance equations (Krijger, 2013 and Lippens, 2014)

This thesis is based on research conducted by Krijger, in 2013, and Lippens, in 2014. They set up the initial system of balances that was extended in this thesis. The balance equations that are unchanged in this thesis are summarised in this appendix.

The underlined text shows which equation pertains to which node. M refers to a mass balance, E to an energy balance, and I to the momentum balance. There is only a single momentum balance for the entire loop, but the mass and energy balances are specified for each node individually. This is indicated by the inclusion of a letter or digit specifying which node the equation governs. A key for which character refers to which node is included in the nomenclature, under *Subscripts*.

As before, the dimensionless variant of variable X is denoted $\underline{X}$, the steady-state value $\overline{X}$, and the perturbation $\check{x}$.

B.1. Transport balances – low heating model

$$\underline{\text{M0:}} \qquad AL\frac{\mathrm{d}}{\mathrm{d}t}\rho_0 = W_0 - W_{out} \tag{B.1}$$

$$\underline{\text{MR:}} \qquad AL_R\frac{\mathrm{d}}{\mathrm{d}t}\rho_R = W_{out} - W_R \tag{B.2}$$

$$\underline{\text{MB:}} \qquad \rho_{in}\frac{\mathrm{d}}{\mathrm{d}t}V_B = W_R - W_0 \tag{B.3}$$

$$\underline{\text{E0:}} \qquad AL\frac{\mathrm{d}}{\mathrm{d}t}\rho_0 H_0 = W_0 H_{in} - W_{out}H_{out} + \frac{Nu_0\lambda_{f,0}}{D_H}P_{in}L(T_w - T_0) \tag{B.4}$$

$$\underline{\text{ER:}} \qquad AL_R\frac{\mathrm{d}}{\mathrm{d}t}\rho_R H_R = W_{out}H_{out} - W_R H_R \tag{B.5}$$

$$\underline{\text{I:}} \qquad AL\frac{\mathrm{d}}{\mathrm{d}t}W_0 + AL_R\frac{\mathrm{d}}{\mathrm{d}t}W_R + \frac{\mathrm{d}}{\mathrm{d}t}V_B W_0 + AL_D\frac{\mathrm{d}}{\mathrm{d}t}W_0 = \cdots$$
$$\cdots - \left(\frac{f_0 L}{D_H} + K_0\right)\frac{W_0^2}{2\rho_0} - \left(\frac{f_R L_R}{D_H} + K_R\right)\frac{W_R^2}{2\rho_R}\cdots$$
$$\cdots - \left(\frac{f_D L_D}{D_H} + K_D\right)\frac{W_0^2}{2\rho_{in}} - A^2 g\rho_0 L - A^2 g\rho_R L_R - A^2 g\rho_{in}L_D \tag{B.6}$$

B.2. Transport balances – high heating model

$$\underline{\text{M0:}} \qquad A\rho_0 \frac{\mathrm{d}}{\mathrm{d}t}L_0 = W_0 - W_{pc} \tag{B.7}$$

$$\underline{\text{M1:}} \qquad A\frac{\mathrm{d}}{\mathrm{d}t}\rho_1 L_1 = W_{pc} - W_1 \tag{B.8}$$

$$\underline{\text{MR:}} \qquad AL_R\frac{\mathrm{d}}{\mathrm{d}t}\rho_R = W_1 - W_R \tag{B.9}$$

$$\underline{\text{MB:}} \qquad \rho_{in}\frac{\mathrm{d}}{\mathrm{d}t}V_B = W_R - W_0 \tag{B.10}$$

$$\underline{\text{E0:}} \qquad A\rho_0 H_0\frac{\mathrm{d}}{\mathrm{d}t}L_0 = W_0 H_{in} - W_{pc}H_{pc} + \frac{Nu_0\lambda_f}{D_H}P_{in}L_0(T_w, 0 - T_0) \tag{B.11}$$

$$\underline{\text{E1:}} \qquad A\frac{\mathrm{d}}{\mathrm{d}t}\rho_1 L_1 H_1 = W_{pc}H_{pc} - W_1 H_1 + \frac{Nu_1\lambda_f}{D_H}P_{in}L_1(T_w, 1 - T_1) \tag{B.12}$$

$$\underline{\text{ER:}} \qquad AL_R\frac{\mathrm{d}}{\mathrm{d}t}\rho_R H_R = W_1 H_1 - W_R H_R \tag{B.13}$$

$$\underline{\text{I:}} \qquad A\frac{\mathrm{d}}{\mathrm{d}t}W_0 L_0 + A\frac{\mathrm{d}}{\mathrm{d}t}W_1 L_1 + AL_R\frac{\mathrm{d}}{\mathrm{d}t}W_R + \frac{\mathrm{d}}{\mathrm{d}t}V_B W_0 + AL_D\frac{\mathrm{d}}{\mathrm{d}t}W_0 = \cdots$$

$$\cdots - \left(\frac{f_0 L_0}{D_H} + K_0\right)\frac{W_0^2}{2\rho_0} - \left(\frac{f_1 L_1}{D_H} + K_1\right)\frac{W_1^2}{2\rho_1} - \left(\frac{f_R L_R}{D_H} + K_R\right)\frac{W_R^2}{2\rho_R}\cdots$$

$$\cdots - \left(\frac{f_D L_D}{D_H} + K_D\right)\frac{W_0^2}{2\rho_{in}} - A^2 g\rho_0 L_0 - A^2 g\rho_1 L_1\cdots$$

$$\cdots - A^2 g\rho_R L_R - A^2 g\rho_{in}L_D \tag{B.14}$$

B.3. Dimensionless balances – low heating model

$$\underline{\text{M0:}} \qquad \frac{\mathrm{d}}{\mathrm{d}\underline{t}}\underline{\rho_0} = \underline{W_0} - \underline{L_R}\frac{\mathrm{d}}{\mathrm{d}\underline{t}}\underline{\rho_R} - \underline{W_R} \tag{B.15}$$

$$\underline{\text{E0:}} \qquad \frac{\mathrm{d}}{\mathrm{d}\underline{t}}\underline{\rho_0}\underline{H_0} = \underline{W_0}\underline{H_{in}} - \underline{H_{out}}\left(\underline{L_R}\frac{\mathrm{d}}{\mathrm{d}\underline{t}}\underline{\rho_R} + \underline{W_R}\right)\cdots$$

$$+ \widehat{\underline{Nu_0}}\underline{\lambda_{f0}^{0.34}}\frac{\underline{P_{in}}}{\underline{D_H}}\left(\underline{T_w} - \underline{T_{pc}} - \underline{\alpha_0}\left(\underline{H_0} - h_{pc}\right)^2\cdots\right.$$

$$\cdots\left. - \frac{1}{\underline{c_{p,pc}}}\left(\underline{H_0} - h_{pc}\right)\right) \tag{B.16}$$

$$\underline{\text{ER:}} \qquad \underline{L_R}\frac{\mathrm{d}}{\mathrm{d}\underline{t}}\underline{\rho_R}\underline{H_R} = \underline{H_{out}}\left(\underline{L_R}\frac{\mathrm{d}}{\mathrm{d}\underline{t}}\underline{\rho_R} + \underline{W_R}\right) - \underline{W_R}\underline{H_R} \tag{B.17}$$

$$\underline{\text{I:}} \qquad \frac{\mathrm{d}}{\mathrm{d}\underline{t}}\underline{W_0} + \underline{L_R}\frac{\mathrm{d}}{\mathrm{d}\underline{t}}\underline{W_R} + \underline{V_B}\frac{\mathrm{d}}{\mathrm{d}\underline{t}}\underline{W_0} + \underline{L_D}\frac{\mathrm{d}}{\mathrm{d}\underline{t}}\underline{W_0} =$$

$$- \underline{W_0}\frac{\underline{W_R} - \underline{W_0}}{\underline{\rho_{in}}} - \left(\frac{\underline{f_0}}{\underline{D_H}} + K_0\right)\frac{\underline{W_0^2}}{2\underline{\rho_0}} - \left(\frac{\underline{f_R}\underline{L_R}}{\underline{D_H}} + K_R\right)\frac{\underline{W_R^2}}{2\underline{\rho_R}}\cdots$$

$$\cdots - \left(\frac{\underline{f_D}\underline{L_D}}{\underline{D_H}} + K_D\right)\frac{\underline{W_0^2}}{2\underline{\rho_{in}}} - \frac{\underline{\rho_0}\underline{L_0}}{N_{Fr}} - \frac{\underline{\rho_R}\underline{L_R}}{N_{Fr}} + \frac{\underline{\rho_{in}}\underline{L_D}}{N_{Fr}} \tag{B.18}$$

B.4. Dimensionless balances – high heating model

$$\underline{\text{M0:}} \quad \underline{\rho_0}\left(\frac{\underline{H_0}}{\overline{\overline{h_{pc}}}} - 1\right)\frac{\text{d}}{\text{d}\underline{t}}\underline{L_1} = \left(1 - \frac{\underline{H_{in}}}{\overline{\overline{h_{pc}}}}\right)\underline{W_0} - \frac{1}{\overline{\overline{h_{pc}}}}(1 - \underline{L_1}) \tag{B.19}$$

$$\underline{\text{M1:}} \quad \left(\underline{\rho_1} - \frac{\underline{H_0}}{\overline{\overline{h_{pc}}}}\underline{\rho_0}\right)\frac{\text{d}}{\text{d}\underline{t}}\underline{L_1} + \underline{L_1}\frac{\text{d}}{\text{d}\underline{t}}\underline{\rho_1} = \frac{\underline{H_{in}}}{\overline{\overline{h_{pc}}}}\underline{W_0} + \frac{1}{\overline{\overline{h_{pc}}}}(1 - \underline{L_1}) - \underline{W_1} \tag{B.20}$$

$$\underline{\text{MR:}} \quad \underline{L_R}\frac{\text{d}}{\text{d}\underline{t}}\underline{\rho_R} = \underline{W_1} - \underline{W_R} \tag{B.21}$$

$$\underline{\text{E1:}} \quad \underline{L_1}\frac{\text{d}}{\text{d}\underline{t}}\underline{\rho_1 H_1} + (\underline{\rho_1 H_1} - \underline{\rho_0 H_0})\frac{\text{d}}{\text{d}\underline{t}}\underline{L_1} = \underline{W_0 H_{in}} - \underline{W_1 H_1} \cdots$$

$$\cdots + \widehat{\underline{Nu_0}}\underline{\lambda_{f0}^{0.34}}\frac{\underline{P_{in}}(1 - \underline{L_1})}{\underline{D_H}}\left(\underline{T_{w,0}} - \underline{T_{pc}} - \underline{\alpha_0}\left(\underline{H_0} - \overline{\overline{h_{pc}}}\right)^2 \cdots\right.$$

$$\cdots - \frac{1}{\underline{c_{p,pc}}}\left(\underline{H_0} - \overline{\overline{h_{pc}}}\right)\bigg)\cdots$$

$$\cdots + \widehat{\underline{Nu_1}}\underline{\lambda_{f1}^{0.34}}\frac{\underline{P_{in}}\underline{L_1}}{\underline{D_H}}\left(\underline{T_{w,1}} - \underline{T_{pc}} - \underline{\alpha_1}\left(\underline{H_1} - \overline{\overline{h_{pc}}}\right)^2 \cdots\right.$$

$$\cdots - \frac{1}{\underline{c_{p,pc}}}\left(\underline{H_1} - \overline{\overline{h_{pc}}}\right)\bigg) \tag{B.22}$$

$$\underline{\text{ER:}} \quad \underline{L_R}\frac{\text{d}}{\text{d}\underline{t}}\underline{\rho_R H_R} = \underline{W_1 H_1} - \underline{W_R H_R} \tag{B.23}$$

$$\underline{\text{I:}} \quad -\underline{W_0}\frac{\text{d}}{\text{d}\underline{t}}\underline{L_1} + (1 - \underline{L_1})\frac{\text{d}}{\text{d}\underline{t}}\underline{W_0} + \frac{\text{d}}{\text{d}\underline{t}}\underline{W_1 L_1} + \underline{L_R}\frac{\text{d}}{\text{d}\underline{t}}\underline{W_R} + \underline{V_B}\frac{\text{d}}{\text{d}\underline{t}}\underline{W_0} + \underline{L_D}\frac{\text{d}}{\text{d}\underline{t}}\underline{W_0} = \cdots$$

$$-\underline{W_0}\frac{\underline{W_R} - \underline{W_0}}{\underline{\rho_{in}}} - \left(\frac{\underline{f_0 L_0}}{\underline{D_H}} + \underline{K_0}\right)\frac{\underline{W_0^2}}{2\underline{\rho_0}} - \left(\frac{\underline{f_1 L_1}}{\underline{D_H}} + \underline{K_1}\right)\frac{\underline{W_1^2}}{2\underline{\rho_1}} \cdots$$

$$\cdots - \left(\frac{\underline{f_R L_R}}{\underline{D_H}} + \underline{K_R}\right)\frac{\underline{W_R^2}}{2\underline{\rho_R}} - \left(\frac{\underline{f_D L_D}}{\underline{D_H}} + \underline{K_D}\right)\frac{\underline{W_0^2}}{2\underline{\rho_{in}}} \cdots$$

$$\cdots - \frac{\underline{\rho_0 L_0}}{\underline{N_{Fr}}} - \frac{\underline{\rho_1 L_1}}{\underline{N_{Fr}}} - \frac{\underline{\rho_R L_R}}{\underline{N_{Fr}}} + \frac{\underline{\rho_{in} L_D}}{\underline{N_{Fr}}} \tag{B.24}$$

B.5. Linearised balances – low heating model

$$\underline{M0:} \quad C_1 N_{\Delta h} h_{pc} v_{pc} \left(\frac{1}{2} \frac{\mathrm{d}}{\mathrm{d}\underline{t}} \check{\underline{h}}_{out} + \underline{L_R} \frac{\mathrm{d}}{\mathrm{d}\underline{t}} \check{\underline{h}}_R \right) = \check{\underline{w}}_0 - \check{\underline{w}}_R \tag{B.25}$$

$$\underline{E0:} \quad \left(\frac{1}{2} \overline{\underline{\rho}}_0 + \frac{1}{2} C_1 N_{\Delta h} h_{pc} v_{pc} \overline{\underline{H}}_0 \right) \frac{\mathrm{d}}{\mathrm{d}\underline{t}} \check{\underline{h}}_{out} + C_1 N_{\Delta h} h_{pc} v_{pc} \overline{\underline{H}}_{out} \underline{L_R} \frac{\mathrm{d}}{\mathrm{d}\underline{t}} \check{\underline{h}}_R =$$

$$- \check{\underline{w}}_R \overline{\underline{H}}_{out} + \check{\underline{w}}_0 \overline{\underline{H}}_{in} + \widehat{Nu_0} \overline{\overline{\underline{\lambda}}}_{f0}^{-0.34} \frac{P_{in}}{\underline{D_H}} \check{\underline{\theta}}_w \cdots$$

$$\cdots - \left(\widehat{Nu_0} \frac{P_{in}}{\overline{\overline{\underline{D_H}}}} \left(\left(\alpha_0 \left(H_0 - h_{pc} \right) + \frac{1}{2\underline{c_{p,pc}}} \right) \overline{\underline{\lambda}}_{f0}^{-0.34} \cdots \right.$$

$$\cdots \left. - 0.17 \overline{\underline{\lambda}}_{f0}^{-0.66} \left(\overline{\underline{T}}_w - \overline{\underline{T}}_0 \right) \beta_0 \right) + 1 \right) \check{\underline{h}}_{out} \tag{B.26}$$

$$\underline{ER:} \quad \left(\underline{L_R} \overline{\underline{\rho}}_R - \underline{L_R} C_1 N_{\Delta h} h_{pc} v_{pc} (\overline{\underline{H}}_R - \overline{\underline{H}}_{out}) \right) \frac{\mathrm{d}}{\mathrm{d}\underline{t}} \check{\underline{h}}_R =$$

$$\check{\underline{h}}_{out} + \overline{\underline{H}}_{out} \check{\underline{w}}_R - \check{\underline{h}}_R - \check{\underline{w}}_R \overline{\underline{H}}_R \tag{B.27}$$

$$\underline{I:} \quad (1 + \underline{L_D} + \underline{V}_B) \frac{\mathrm{d}}{\mathrm{d}\underline{t}} \check{\underline{w}}_0 + \underline{L_R} \frac{\mathrm{d}}{\mathrm{d}\underline{t}} \check{\underline{w}}_R = - \left(\left(\frac{f_R \underline{L_R}}{\underline{D_H}} + K_R \right) \overline{\underline{v}}_R + v_{in} \right) \check{\underline{w}}_R \cdots$$

$$\cdots + \frac{1}{2} C_1 N_{\Delta h} h_{pc} v_{pc} \left(\frac{1}{2} \left(\frac{f_0}{\underline{D_H}} + K_0 \right) \frac{1}{\overline{\underline{\rho}}_0^2} - \frac{1}{N_{Fr}} \right) \check{\underline{h}}_{out} \cdots$$

$$\cdots + \frac{1}{2} C_1 N_{\Delta h} h_{pc} v_{pc} \left(\frac{1}{2} \left(\frac{f_R \underline{L_R}}{\underline{D_H}} + K_R \right) \frac{1}{\overline{\underline{\rho}}_R^2} - \frac{\underline{L_R}}{N_{Fr}} \right) \check{\underline{h}}_R \cdots$$

$$\cdots \left(v_{in} \left(\frac{f_0}{\underline{D_H}} + K_0 \right) \overline{\underline{v}}_0 - \left(\frac{f_D \underline{L_D}}{\underline{D_H}} + K_D \right) v_{in} \right) \check{\underline{w}}_0 \tag{B.28}$$

B.6. Linearised balances – high heating model

$$\underline{\text{M0:}}\qquad \rho_0\left(\frac{H_0}{h_{pc}} - 1\right)\frac{d}{dt}\breve{l}_1 = \left(1 - \frac{H_{in}}{h_{pc}}\right)\breve{w}_0 + \frac{1}{h_{pc}}\breve{l}_1 \tag{B.29}$$

$$\underline{\text{M1:}}\qquad \left(\frac{1}{\overline{v}_1} - \frac{H_0}{h_{pc}}\rho_0\right)\frac{d}{dt}\breve{l}_1 - \frac{\overline{L}_1 C_1 N_{\Delta h} h_{pc}}{vpc\,\overline{v}_1^2}\frac{d}{dt}\breve{h}_1 =$$

$$\frac{H_{in}}{h_{pc}}\breve{w}_0 - \frac{1}{h_{pc}}\breve{l}_1 - \breve{w}_1 \tag{B.30}$$

$$\underline{\text{MR:}}\qquad -\frac{\overline{L}_R C_1 N_{\Delta h} h_{pc}}{vpc\,\overline{v}_R^2}\frac{d}{dt}\breve{h}_R = \breve{w}_1 - \breve{w}_R \tag{B.31}$$

$$\underline{\text{E1:}}\qquad \frac{\overline{L}_1}{\overline{v}_1}\left(1 - \frac{\overline{H}_1 C_1 N_{\Delta h} h_{pc}}{vpc\,\overline{v}_1}\right)\frac{d}{dt}\breve{h}_1 + \left(\frac{\overline{H}_1}{\overline{v}_1} - H_0\rho_0\right)\frac{d}{dt}\breve{l}_1 =$$

$$H_{in}\breve{w}_0 - \overline{H}_1\breve{w}_1 + \widehat{Nu_0}\,\overline{\lambda}_{f0}^{-0.34}\frac{P_{in}\overline{L}_0}{D_H}\breve{\theta}_{w,0}\cdots$$

$$\cdots -\left(\widehat{Nu_1}\frac{P_{in}\overline{L}_1}{D_H}\left(\left(2\alpha_1\left(\overline{H}_1 - h_{pc}\right) + \frac{1}{c_{p,pc}}\right)\overline{\lambda}_{f1}^{-0.34}\cdots\right.\right.$$

$$\cdots + 0.34\left(\overline{T}_{w,1} - \overline{T}_1\right)\overline{\lambda}_{f1}^{-0.66}\beta_1\lambda_z e^{-\beta_1\overline{H}_1}\right) + 1\Big)\breve{h}_1\cdots$$

$$\cdots + \widehat{Nu_1}\,\overline{\lambda}_{f1}^{-0.34}\frac{P_{in}\overline{L}_1}{D_H}\breve{\theta}_{w,1} + \frac{P_{in}}{D_H}\left(\widehat{Nu_1}\,\overline{\lambda}_{f1}^{-0.34}\left(\overline{T}_{w,1} - \overline{T}_1\right)\cdots\right.$$

$$\cdots -\widehat{Nu_0}\,\overline{\lambda}_{f0}^{-0.34}\left(\overline{T}_{w,0} - \overline{T}_0\right)\Big)\breve{l}_1 \tag{B.32}$$

$$\underline{\text{ER:}}\qquad \frac{\overline{L}_R}{\overline{v}_R}\left(1 - \frac{\overline{H}_R C_1 N_{\Delta h} h_{pc}}{vpc\,\overline{v}_R}\right)\frac{d}{dt}\breve{h}_R = \breve{h}_1 + \overline{H}_1\breve{w}_1 - \breve{h}_R - \overline{H}_R\breve{w}_R \tag{B.33}$$

$$\underline{\text{I:}}\qquad (1 + \overline{L}_1 + L_D + V_B)\frac{d}{dt}\breve{w}_0 + L_1\frac{d}{dt}\breve{w}_1 + L_R\frac{d}{dt}\breve{w}_R =$$

$$\left(\frac{1}{2}\left(\frac{f_0 v_0}{D_H} - \frac{f_1\overline{v}_1}{D_H}\right) + \frac{1}{N_{Fr}v_0} - \frac{1}{N_{Fr}\overline{v}_1}\right)\breve{l}_1\cdots$$

$$\cdots -\left(\left(\frac{f_0\overline{L}_0}{D_H} + K_0\right)\overline{v}_0\left(\frac{f_D\overline{L}_D}{D_H} + K_D\right)\overline{v}_{in} - v_{in}\right)\breve{w}_0\cdots$$

$$\cdots -\left(\frac{f_1\overline{L}_1}{D_H} + K_1\right)\overline{v}_1\breve{w}_1 + \left(-\frac{1}{2}\left(\frac{f_1\overline{L}_1}{D_H} + K_1\right)\cdots\right.$$

$$\cdots +\frac{\overline{L}_1}{N_{Fr}\overline{v}_R^2}\right)\frac{C_1 N_{\Delta h} h_{pc}}{vpc}\breve{h}_1\cdots$$

$$\cdots -\left(\frac{f_R\overline{L}_R}{D_H} + K_R + \frac{v_{in}}{\overline{v}_R}\right)\overline{v}_R\breve{w}_R + \left(-\frac{1}{2}\left(\frac{f_R\overline{L}_R}{D_H} + K_R\right)\cdots\right.$$

$$\cdots +\frac{\overline{L}_R}{N_{Fr}\overline{v}_R^2}\right)\frac{C_1 N_{\Delta h} h_{pc}}{vpc}\breve{h}_R \tag{B.34}$$

C

Reference case parameters and constants

Krijger [1] set up a reference case for the model used in this thesis as baseline for comparison. Lippens [2] extended the reference case for the additions he made to the code. The reference case is now also extended with parameters governing the neutronics of the system.

Table C.1: Design parameters for the reference case

Parameter	Value
Volume buffer vessel	$10^{-2}\mathrm{m}^3$
Riser length	4.2m
Core length	4.2m
Channel hydraulic diameter	$5.6 \cdot 10^{-3}\mathrm{m}$
Channel flow area	$3.55 \cdot 10^{-5}\mathrm{m}^2$
Wall cross-sectional area	$3.55 \cdot 10^{-5}\mathrm{m}^2$
Fuel volume per rod	$1.48 \cdot 10^{-4}\mathrm{m}^3$
Inlet pressure loss coefficient	1
Downcomer pressure loss coefficient	1
Riser pressure loss coefficient	20

Table C.2: Material, thermodynamic and neutronic properties for the reference case

Property	Value
Water specific enthalpy, pseudo-critical point	$2.1529 \cdot 10^6 \mathrm{J\ kg^{-1}}$
Water specific volume, pseudo-critical point	$3.1564 \cdot 10^{-3}\mathrm{m}^3\ \mathrm{kg^{-1}}$
Water specific heat capacity, pseudo-critical point	$7.6444 \cdot 10^4\ \mathrm{J\ kg^{-1}\ K^{-1}}$
Dynamic viscosity of water	$4.2797 \cdot 10^{-5}\ \mathrm{N\ s\ m^{-2}}$
Fuel density	$10.96 \cdot 10^3 \mathrm{kg\ m^{-3}}$
Wall density	$7.850 \cdot 10^3 \mathrm{kg\ m^{-3}}$
Wall specific heat capacity	$490\ \mathrm{J\ kg^{-1}\ K^{-1}}$
Wall thermal conductivity	$43\ \mathrm{W\ m^{-1}\ K^{-1}}$
Fuel heat transfer time constant	6 s
Energy per fission event	$2.81 \cdot 10^{-11}\mathrm{J}$
Fuel enrichment	4% by mass
Neutron velocity	$5.72958 \cdot 10^3\ \mathrm{m\ s^{-1}}$

Table C.3: Delayed neutron fractions and decay constants [22]

Fractions (%)		Decay constants (s^{-1})	
β_1	0.026	λ_1	0.0127
β_2	0.1459	λ_2	0.0317
β_3	0.1288	λ_3	0.115
β_4	0.2788	λ_4	0.311
β_5	0.0877	λ_5	1.40
β_6	0.0178	λ_6	3.87

Bibliography

[1] D. Krijger, *A linear stability analysis of a water loop driven by natural convection at supercritical conditions,* (2013).

[2] G. Lippens, *Linear analysis of thermal inertia effects on the thermal-hydraulic stability of a natural circulation driven supercritical water loop,* (2014).

[3] T. Ortega Gómez, *Stability Analysis of the High Performance Light Water Reactor*, Ph.D. thesis, Institut für Kern- und Energietechnik, Universität Karlsruhe (2009).

[4] *Gif–technology–systems,* Generation IV International Forum (2014), accessed 10 July 2014.

[5] *Supercritical-water-cooled reactor (scwr),* Generation IV International Forum (2014), accessed 10 July 2014.

[6] S. J. H. J. Schulenberg, T., *Three pass core design proposal for a high performance light water reactor,* Progress in Nuclear Energy **50**, 526 (2007).

[7] J. Spoelstra, *Numerical stability analysis of natural circulation driven supercritical water reactors*, Master's thesis, Delft University of Technology (2012).

[8] *Thermophysical properties of fluid systems,* National Institute of Science and Technology (2014), accessed 15 July 2014.

[9] J. Bouré, A. Bergles, and L. Tong, *Review of two-phase flow instability,* Nuclear Engineering and Design **25**, 165 (1973).

[10] D. Van Bragt, *Analytical Modeling of Boiling Water Reactor Dynamics*, Ph.D. thesis, Department of Reactor Physics, Delft University of Technology (1998).

[11] S. Lomperski, D. Cho, R. Jain, and M. Corradini, *Stability of a natural circulation loop with a fluid heated through the thermodynamic pseudo-critical point,* in *Proceedings of the 2004 International Congress on Advances in Nuclear Power Plants, ICAPP'04* (2004) pp. 1736–1741.

[12] V. Chatoorgoon, A. Voodi, and D. Fraser, *The stability boundary for supercritical flow in natural convection loops, part i: H_2o studies,* Nuclear Engineering and Design **235**, 2570 (2005).

[13] P. Jain and Rizwan-uddin, *Numerical analysis of supercritical flow instabilities in a natural circulation loop,* Nuclear Engineering and Design **238**, 1947 (2008).

[14] C. T'Joen and M. Rohde, *Experimental study of the coupled thermo-hydraulic-neutronic stability of a natural circulation hplwr,* Nuclear Engineering and Design **242**, 221 (2012).

[15] F. Kam, *Development of a one-dimensional model for the stability analysis of a natural circulation Super Critical Water Reactor*, Master's thesis, Delft University of Technology (2011).

[16] T. Schenderling, *Numerical analysis of the influence of wall thermal inertia on the stability of natural circulation driven supercritical water reactors,* (2013).

[17] G. Guido, J. Converti, and A. Clausse, *Density-wave oscillations in parallel channels – an analytical approach,* Nuclear Engineering and Design **125**, 121 (1991).

[18] T. Van der Hagen, *Experimental and theoretical evidence for a short effective fuel time constant in a boiling water reactor,* Nuclear Technology **83**, 171 (1988).

[19] M. Schlagenhaufer, *Reactivity control mechanisms for a hplwr fuel assembly,* in *Proceedings of Global 2007, Boise, Idaho, USA, September 9–13* (2007).

[20] *Eigenvalues and eigenvectors,* MATLAB Documentation (2014), accessed 11 July 2014.

[21] G. Koren, *Linear stability analysis of a supercritical water loop driven by natural convection,* (2010).

[22] H. Van Dam, T. Van der Hagen, and J. Hoogenboom, *Nuclear reactor physics — lecture notes,* (2004).